Monthly Sea-Surface Temperature, Sea Ice, and Sea-Level Pressure from 1850–2023 using Coupled Atmosphere–Ocean Data Assimilation

Vincent T. Cooper,[a]

[a] *Department of Atmospheric and Climate Science, University of Washington, Seattle, WA, USA*

Corresponding author: Vincent T. Cooper, vcooper@uw.edu

ABSTRACT: Historical observations of Earth's climate underpin our knowledge and predictions of climate variability and change. However, historical datasets are often inconsistent due to sparse, error-prone instrumental data, which limits understanding of climate dynamics. Combining linear inverse models (LIMs) with coupled data assimilation presents an opportunity to reconstruct and quantify uncertainty in globally resolved sea-surface temperature (SST), near-surface air temperature (T), sea-level pressure (SLP), and sea-ice concentration (SIC), with dynamical constraints. Here, we present a monthly resolved reconstruction using coupled data assimilation with LIMs from 1850–2023. We train LIMs on eight CMIP6 models to forecast the climate state and its error covariance, and we assimilate observations of SST, land T, marine SLP, and satellite-era SIC using the classic Kalman filter. We quantify uncertainty in model physics, observations, and bias corrections with 1600 ensemble members, and we validate the method by reconstructing an out-of-sample climate model. Key findings in the Tropics include post-1980 trends in the Walker circulation and zonal-Pacific SST gradient that are consistent with past variability, whereas the tropical SST contrast (the difference between warmer and colder SSTs) shows a consistent strengthening since 1975. ENSO amplitude exhibits substantial low-frequency variability and a local maximum in variance from 1875–1910. In polar regions, we find a muted cooling trend in the Southern Ocean post-1980 and substantial uncertainty. Changes in Antarctic sea ice are relatively small between 1850 and 2000, while Arctic sea ice declines by 0.5 ± 0.1 (1σ) million km^2 during the 1920s.

1. Introduction

The historical record (c. 1850–present) is central to our understanding of climate variability and Earth's response to anthropogenic forcings, but we have yet to fully extract the available information from instrumental data. Observations of sea-surface temperature (SST), near-surface air temperature (T), and sea-level pressure (SLP) from ships of opportunity and weather stations are noisy, sparse, and vary over time, which adds an incomplete-data problem (Schneider 2001) to analyses of climate variability and change that cannot be avoided and should not be ignored.

The homogenization of instrumental observations (Kent and Kennedy 2021; Chan and Huybers 2019; Chan et al. 2023; Karl et al. 2015; Hausfather et al. 2017) and imputation of missing values have pronounced impacts on assessments of the climate sensitivity to increasing greenhouse gases (Sherwood et al. 2020; Forster et al. 2021), on efforts to distinguish internal variability from forced climate change (Schneider and Held 2001; Hegerl et al. 2019), and on our general quantification of atmosphere–ocean variability (Battisti et al. 2019). The evaluation of climate models also depends on comparison with historical datasets (Wills et al. 2022). To improve understanding, we need to synthesize observations across the Earth system using methods that are physically constrained by dynamics.

The pattern effect on climate sensitivity, i.e., the dependence of radiative feedbacks on spatial patterns of SST anomalies (Armour et al. 2013; Andrews et al. 2015; Zhou et al. 2016; Ceppi and Gregory 2017; Andrews and Webb 2018; Fueglistaler 2019; Dong et al. 2019, 2020; Cooper et al. 2024), is a salient problem in climate dynamics with strong ties to the incomplete-data problem. The pattern effect over the historical record (Andrews et al. 2018, 2022; Marvel et al. 2018; Salvi et al. 2023) depends on what the SST patterns were in the past, and recent studies have revealed that differences across infilled SST datasets lead to disparate interpretations of the historical pattern effect (Fueglistaler and Silvers 2021; Lewis and Mauritsen 2021), or possibly no pattern effect at all (Modak and Mauritsen 2023). This study is strongly motivated by the need to improve constraints on past SST patterns, on the historical pattern effect, and on many aspects of large-scale climate dynamics that are coupled to SST variability.

SST patterns play a ubiquitous role in regulating climate variability, cloud feedbacks, and the atmospheric circulation (Deser et al. 2010). There are a variety of recent (c. 1980–present) climate phenomena tied to SSTs that seem either unprecedented or unremarkable depending on what we deem to be natural variability, and this interpretation of recent trends relies on the incomplete instrumental record (Wunsch 1999; Kaplan et al. 1998). In the Tropics, there have been perplexing changes in SST gradients (Fueglistaler and Silvers 2021; Solomon and Newman 2012; Coats and Karnauskas 2017; Lee et al. 2022; Watanabe et al. 2024), the Walker circulation (Vecchi et al. 2006; L'Heureux et al. 2013; McGregor et al. 2014; Watanabe et al. 2023; Tokinaga et al. 2012), and tropospheric temperatures coupled to SST patterns (Flannaghan et al. 2014; Fueglistaler 2019).

The Southern Ocean is receiving increasing attention for its pronounced influence on global climate and cloud feedbacks (Kang et al. 2023b,a; Dong et al. 2022; Hartmann 2022), and there is an ongoing struggle to explain the post-1980 cooling trend in the Southern Ocean and to understand why climate models cannot reproduce the magnitude of cooling in the NOAA ERSST dataset (Huang et al. 2017; Blanchard-Wrigglesworth et al. 2021; Dong et al. 2023). Antarctic sea ice also has a substantial impact on radiative feedbacks (SI of Andrews et al. 2018) and continues to follow an unexpected trajectory (Fogt et al. 2022), but we know little about its evolution prior to the satellite era (Fan et al. 2014).

Furthermore, understanding of the early-twentieth-century warming (ETCW) in the Arctic (Brönnimann 2009; Hegerl et al. 2018) and the possible loss of Arctic sea ice between the 1910s and 1940s, which appears in Brennan and Hakim (2022) and Walsh et al. (2017) but not in HadISST nor HadISST2 (Rayner et al. 2003; Titchner and Rayner 2014), has been limited by the paucity of Arctic observations. Could innovative analysis of instrumental data resolve these unknown aspects of historical variability?

Existing SST datasets designed for climate analysis use a variety of statistical interpolation methods. These methods have been recently summarized in Modak and Mauritsen (2023) and Lewis and Mauritsen (2021) and described in detail in a review by Kent and Kennedy (2021), which also explains the extensive efforts to homogenize time-varying sources of in situ data. To assess radiative feedbacks over the historical record in atmospheric general circulation models (i.e., in AMIP-type simulations), complete coverage and monthly resolution of SST and sea-ice concentration (SIC) is required. Combined SST and SIC datasets for this purpose include the PCMDI AMIP II boundary condition from 1870–2017 (Hurrell et al. 2008) used as the standard for CMIP6, NOAA ERSSTv5 from 1854–present (Huang et al. 2017), Met Office Hadley Centre's HadISST1 from 1870–present (Rayner et al. 2003) and HadISST2.1 (no longer maintained) from

1850–2010 (Titchner and Rayner 2014), and the Japanese Meteorological Agency COBE-SST2 from 1850–present (Hirahara et al. 2014). Since Kaplan et al. (1998) developed a landmark SST analysis using optimal interpolation, the incomplete-data problem has been investigated using kriging (Cowtan and Way 2014), and Vaccaro et al. (2021) used Markov random graphs while Kadow et al. (2020) used machine learning to impute hybrid air-sea surface temperatures over land and ocean.

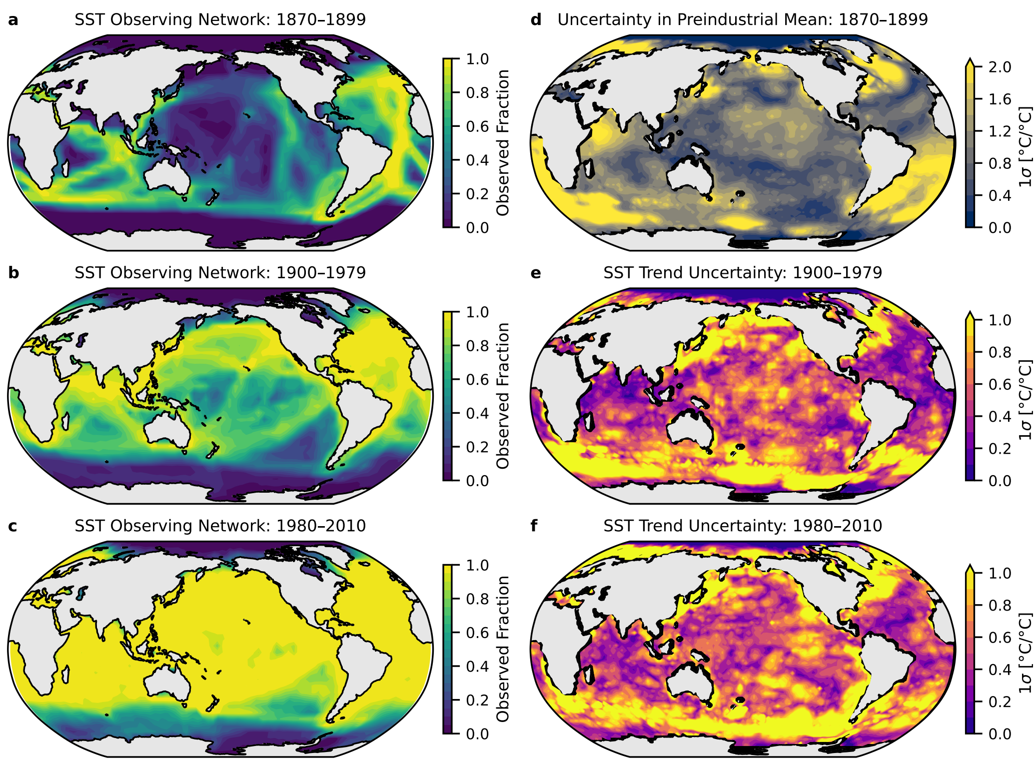

FIG. 1. **Historical observing network and SST uncertainty in pre-existing infilled datasets. (a–c)** Fraction of months with in situ data for SST over three time periods in HadSST4, where 1.0 indicates data in every month during the period. **(d)** Illustration of systematic uncertainty in normalized pattern of preindustrial-mean SST anomalies in existing infilled datasets, calculated as the sample standard deviation (1σ) of the 1870–1899 mean anomalies across HadISST1, HadISST2.1, ERSSTv5, PCMDI/AMIP II, and COBE-SST2, relative to their 1961–1990 climatologies; local anomalies are divided by global-mean anomalies (60°S–60°N) to highlight uncertainty in spatial patterns. **(e–f)** Illustration of systematic uncertainty in patterns of SST trends, calculated as the 1σ of local trends across the same datasets in panel **d**; local SST trends are first divided by the global-mean SST trends (60°S–60°N) to highlight uncertainty in the patterns, and local values greater than 1.0 indicate that the local 1σ is greater than the global-mean trend. Note different colorbars in panels **d–f**.

Figure 1 depicts the time-evolving observing network of in situ SST measurements in HadSST4 (Kennedy et al. 2019). As motivation for this study, we illustrate the spread (1σ) across existing datasets (HadISST1, HadISST2.1, ERSSTv5, COBE-SST2, and AMIPII) in their preindustrial-baseline SST (mean anomaly over years 1870–1899) and the spread in their SST trends from 1900–1979 and 1980–2010. We separate the satellite era (c. 1980–present) from the earlier warming because of the variety of studies highlighting and questioning the peculiarity of recent trends (e.g., Fueglistaler and Silvers 2021; Andrews et al. 2022; Lewis and Mauritsen 2021). The spatial pattern of uncertainty is influenced by varying methods of imputation, homogenization of data sources, and representativeness error in using point observations as estimates of grid-scale means. It may be surprising to see that even post-1980, the data coverage over the Southern Ocean and southeast Pacific is far from complete, and the inter-dataset differences in those regions are notable even in recent decades (Figure 1c,f). Marine observations of sea-level pressure (SLP) have a similar footprint to the SST observing network in Figure 1.

Atmospheric reanalyses address the incomplete-data problem by using data assimilation, but coupled data assimilation of both atmosphere and ocean is still a frontier in climate research. Data assimilation (DA) describes the collection of methods that synthesize model forecasts with sparse and noisy observations, producing posterior analyses and uncertainties that are subject to the dynamical constraints of the model. DA is computationally intensive, hence existing reanalyses only assimilate data in the atmospheric component, meaning that the SST and SIC boundary conditions are prescribed a priori in ERA5 (Hersbach et al. 2020), JRA-55 (KOBAYASHI et al. 2015), NOAA's 20$^{\text{th}}$ Century Reanalysis (Compo et al. 2011; Slivinski et al. 2019), and Mod-ERA (Franke et al. 2017; Valler et al. 2024). Progress in coupled atmosphere–ocean reanalysis has been slow and difficult. ECMWF's coupled DA program, CERA-20C (Laloyaux et al. 2018), is now inactive, and ECMWF no longer hosts the output from CERA-20C.

To circumvent the computational obstacles associated with DA in fully coupled models, lightweight DA methods have been developed primarily for paleoclimate reconstruction. The "offline" DA method uses a static, uninformed prior from pre-existing model output (e.g., Hakim et al. 2016; Steiger et al. 2014, 2018; Tierney et al. 2020; Osman et al. 2021; Smerdon et al. 2023). "Online" methods use a time-evolving prior that is informed by the previous initial conditions produced by data assimilation. Online DA requires integrating a forecast model after each assimilation step, and the expensive forecasting causes a computational bottleneck.

Data-driven approaches that emulate climate models can overcome the computational bottleneck. The linear inverse model (LIM) has been tested in annual-mean DA with proxies over the last millennium (Perkins and Hakim 2021) and for subseasonal forecasting (Hakim et al. 2022). LIMs have been applied to study dynamics and predictability of ENSO (e.g., Penland and Sardeshmukh 1995; Shin et al. 2021; Vimont et al. 2014; Kido et al. 2023), meridional modes (Vimont 2012), global surface temperatures (Newman 2013), SSTs in the North Atlantic (e.g., Zanna 2012) and North Pacific (Newman 2007; Newman et al. 2016; Zhao et al. 2024), hydroclimate (Coats et al. 2020; Tseng et al. 2021), and sea ice (Brennan et al. 2023). LIMs are computationally efficient, enabling coupled assimilation of observations across Earth system components, e.g., pressure observations in the atmosphere and SST observations in the ocean can each inform both SST and SLP in coupled DA. Combining LIMs with data assimilation presents an exciting opportunity to constrain and quantify uncertainty in globally resolved SST, near-surface air temperature (T), SLP, and SIC over the historical record, with physically consistent constraints across the climate state.

The primary goals of this study are to produce an improved reconstruction of monthly SST, T, SLP, and SIC with global coverage from 1850–present and to quantify the time-varying uncertainty. Section 2 describes methods and data, including linear inverse models, data assimilation, validation with an out-of-sample reconstruction, observations, and comparison datasets. Section 3 describes the results of the data assimilation with real observations. Section 4 discusses the implications of the results for interpreting climate variability and the caveats of the method. Section 5 presents the conclusions.

2. Methods and data

In this section, we describe the reconstruction method, our validation testing, and data sources. The reconstruction of monthly means consists of (i) a monthly forecast, for which we use LIMs that emulate eight CMIP6 models, and (ii) data assimilation in every month, for which we use the classic Kalman filter (Kalman 1960; Kalnay 2003). We validate the method with a pseudo-reconstruction of a climate model's 1850–2014 historical simulation (MPI-ESM1-2-HR), from which we draw observations that mimic the true observing network.

a. Linear inverse models

Anomalies around an equilibrium state in the nonlinear climate system can be approximated as a stochastically forced, linear dynamical system (e.g., Hasselmann 1976; Penland and Sardeshmukh 1995; Penland 1996):

$$\frac{d\mathbf{x}}{dt} = \mathbf{L}\mathbf{x} + \mathbf{S}\eta, \tag{1}$$

where $\mathbf{x}$ is a state vector of N principal components of SST, SLP, and SIC, $\mathbf{L}$ is an $N \times N$ linear operator representing the deterministic dynamics, and $\mathbf{S}\eta$ approximates the unresolvable nonlinear dynamics as stochastic forcing with an $N \times M$ noise-amplitude matrix, $\mathbf{S}$, and a vector, η, of independent, Gaussian white noise with unit variance and length M.

LIMs typically assume stationary statistics, but Shin et al. (2021) extend the LIM framework to include monthly variations in the dynamics. The monthly, or "cyclostationary" LIM, has been applied to ENSO (Shin et al. 2021; Vimont et al. 2022; Kido et al. 2023). We build on this recent work and use cyclostationary LIMs to model global SST, T, SLP, and SIC. We use the fixed-phase approach (OrtizBeviá 1997) to train the 12 $\mathbf{L}_j$ operators in the cyclostationary LIM, where j indicates the month:

$$\mathbf{L}_j = \tau^{-1} \log[\mathbf{C}_j(\tau)\mathbf{C}_j(0)^{-1}], \quad \text{for } j = 1, 2, ..., 12. \tag{2}$$

$\mathbf{C}_j(\tau)$ and $\mathbf{C}_j(0)$ are the τ-lag and zero-lag covariance matrices of $\mathbf{x}$ for month j, and $\tau = 1$ month in all of the following equations. The stochastic amplitude matrices, $\mathbf{S}_j$, are estimated from the fluctuation-dissipation relation of Equation (1) (Penland and Matrosova 1994),

$$\frac{d\mathbf{C}_j(0)}{dt} = \mathbf{L}_j\mathbf{C}_j(0) + \mathbf{C}_j(0)\mathbf{L}_j^T + \mathbf{Q}_j, \tag{3}$$

where $\mathbf{Q}_j = \mathbf{S}_j\mathbf{S}_j^T$. We follow Shin et al. (2021) in estimating the cyclostationary $\mathbf{Q}_j$ as

$$\mathbf{Q}_j = \frac{\mathbf{C}_{j+1}(0) + \mathbf{C}_{j-1}(0)}{2\Delta t} - [\mathbf{L}_j\mathbf{C}_j(0) + \mathbf{C}_j(0)\mathbf{L}_j^T], \tag{4}$$

with $\Delta t = 1$ month. Before computing $\mathbf{L}_j$ and $\mathbf{Q}_j$, we follow Shin et al. (2021) in taking the 3-month running means of $\mathbf{C}_j(\tau)$ and $\mathbf{C}_j(0)$, e.g., we estimate $\mathbf{C}_j(\tau) \approx \langle \mathbf{C}_{j-1}(\tau), \mathbf{C}_j(\tau), \mathbf{C}_{j+1}(\tau) \rangle$. As in other LIM studies (e.g., Penland 1996), we remove any negative eigenvalues in $\mathbf{Q}_j$ and rescale remaining eigenvectors to conserve the original variance.

The LIM produces forecasts at lead $\tau = 1$ month from integrating Equation 1 in time as

$$\mathbf{x}(t+\tau) = \mathbf{G}_j \mathbf{x}(t) + \mathbf{n}, \tag{5}$$

where $\mathbf{G}_j = \exp(\mathbf{L}_j \tau) = \mathbf{C}_j(\tau)\mathbf{C}_j(0)^{-1}$. The integrated stochastic term, $\mathbf{n}$, equals 0 in a deterministic forecast, but we cannot ignore this term in data assimilation because of its contribution to the error covariance, $\mathbf{P}(t) = \mathrm{cov}[\mathbf{x}(t), \mathbf{x}(t)]$.

The forecast equation for the error covariance, assuming no correlation between error and state, is

$$\mathbf{P}(t+\tau) = \mathbf{G}_j \mathbf{P}(t) \mathbf{G}_j^T + \mathbf{N}_j(\tau). \tag{6}$$

To solve for $\mathbf{N}_j(\tau)$, we extend the logic that applies to the stationary LIM (Hakim et al. 2022; Penland 1989) for the cyclostationary case. Equation 6 must be valid for any month's initial condition, including $\mathbf{C}_j(0)$, from which the monthly forecast must arrive at $\mathbf{C}_{j+1}(0)$ because the statistics are cyclostationary, therefore:

$$\mathbf{N}_j(\tau) = \mathbf{C}_{j+1}(0) - \mathbf{G}_j \mathbf{C}_j(0) \mathbf{G}_j^T. \tag{7}$$

For the reconstruction, the key equations of the forecast model are Equation 5, which forecasts the mean, and Equation 6, which forecasts the error covariance.

We train separate LIMs to emulate the following eight CMIP6 models: CESM2, GFDL-ESM4, HadGEM3-GC3.1-LL, SAM0-UNICON, UKESM1.0-LL, NorESM2-LM, EC-Earth3, and E3SM-2-0. For training, we use preindustrial-control simulations with the 1850–2014 historical simulations appended. Our selection of models is informed by Lou et al. (2023), which found that this subgroup performs best in an analog method for ENSO forecasting, although we make two changes: we remove HadGEM3-GC3.1-MM to prevent having two versions of HadGEM3, and we substitute E3SMv2.0 (Qin et al. 2024) for CIESM because of issues simulating sea ice in CIESM (Lin et al. 2020). LIM training is summarized in the Appendix. LIMs are trained separately for each model using monthly mean anomalies, and each LIM has a minimum of 665 years of training data (500 preindustrial and 165 historical years).

We regrid all training data to 2° resolution (96×144 latitude-longitude grid). For consistency with observations, which are expressed as anomalies relative to a 1961–1990 climatology, we remove the grand mean and climatological means calculated over 1961–1990 for each model. Separately for each model and state variable, we compute EOFs area-weighted by the square-root of the cosine of latitude for SST, T, SLP, Northern Hemisphere (NH) SIC, and Southern Hemisphere (SH) SIC. We retain approximately 85% of each field's variance in the truncated state (Appendix). We form each model's standardized state vector from its principal components, $\mathbf{x}_k$, as:

$$\mathbf{x} = \begin{bmatrix} \mathbf{x}_{SST}/\sigma_{SST} \\ \mathbf{x}_{T}/\sigma_{T} \\ \mathbf{x}_{SLP}/\sigma_{SLP} \\ \mathbf{x}_{SIC_{NH}}/\sigma_{SIC_{NH}} \\ \mathbf{x}_{SIC_{SH}}/\sigma_{SIC_{SH}} \end{bmatrix},$$

where σ_k^2 is the retained variance after EOF truncation of field k. We use the standardized state vectors $\mathbf{x}$ to compute covariance matrices for each model, and we project into and out of the LIM basis by storing the EOFs and scale factors, σ_k, for each field. Each LIM is run independently in parallel through the data assimilation framework.

b. Data assimilation

Given a prior forecast of the state's monthly mean $\mathbf{x}_f$ and error covariance $\mathbf{P}_f$, we assimilate observations to produce the posterior analysis $\mathbf{x}_a$ and $\mathbf{P}_a$ using the Kalman filter:

$$\mathbf{x}_a = \mathbf{x}_f + \mathbf{K}(\mathbf{y} - \mathbf{H}\mathbf{x}_f), \tag{8}$$

$$\mathbf{P}_a = [\mathbf{I} - \mathbf{K}\mathbf{H}]\mathbf{P}_f, \tag{9}$$

$$\mathbf{K} = \mathbf{P}_f\mathbf{H}^T[\mathbf{H}\mathbf{P}_f\mathbf{H}^T + \mathbf{R}]^{-1}, \tag{10}$$

where $\mathbf{K}$ is the Kalman gain, $\mathbf{y}$ is the vector of observations, $\mathbf{H}$ is the linear observation operator, and $\mathbf{R}$ is the observation error covariance. After solving Equations 8–10 for a given month, we use the posterior analysis as the initial condition in forecasting the next month with Equations 5 and 6.

Our method is "strongly coupled online DA," where "strongly coupled" means that we assimilate observations concurrently across the atmosphere and ocean using cross-component covariances, and "online" means that we use a forecast model with the previous assimilation step's initial conditions to inform the prior. Because this method uses the classic Kalman filter and propagates $\mathbf{P}_f$ exactly, we avoid the sample error and localization issues that arise when estimating $\mathbf{P}_f$ in an ensemble Kalman filter (Evensen 1994; Houtekamer and Zhang 2016). The downside of this method is that we cannot analyze statistics of temporal variability without ensemble members.

To solve that problem, we generate ensemble members as though we were using the ensemble Kalman filter with perturbed observations (Houtekamer and Mitchell 1998; Burgers et al. 1998), but instead of using the ensemble members to estimate $\mathbf{P}_f$, we use the exact forecast from the classic Kalman filter. For each LIM, we initialize 200 ensemble members in January 1850 with random draws from a multivariate-normal distribution with covariance $\mathbf{C}_1(0)$. Each ensemble member is updated using Equation 8, with $\mathbf{x}_f^n$ corresponding to ensemble member n in place of the ensemble mean, and $\mathbf{y}^n$ is a multivariate-normal random draw of the observations with mean $\mathbf{y}$ and covariance $\mathbf{R}$. After the assimilation, each $\mathbf{x}_a^n$ is advanced to the next month using Equation 5. The noise term in Equation 5, $\mathbf{n}$, becomes a random draw from $\mathbf{N}_j(\tau)$ in Equation 7 for each ensemble member. Because our LIMs are built to forecast monthly means, we can draw from the distributions of the monthly statistics rather than stochastically integrating (Penland and Matrosova 1994) each ensemble member.

An additional benefit of the ensemble is that we can propagate temporally correlated observation errors that are associated with uncertainties in bias corrections. For example, HadSST4 (described below) provides a 200-member ensemble of monthly SST observations to represent temporally correlated errors (Kennedy et al. 2019). To incorporate these errors, we let $\mathbf{y}$ vary across the ensemble members, but each of our 200 ensemble members $\mathbf{x}^n$ is paired at every timestep with the corresponding ensemble member n from the HadSST4 ensemble.

c. Observations

We use four sources of observations corresponding to each of the four state variables (SST, T, SLP, SIC). All observations are anomalies relative to a 1961–1990 climatology, which is the period chosen by Kennedy et al. (2019) and Osborn et al. (2021).

SST observations are from HadSST4 version 4.0.1.0 (Kennedy et al. 2019), provided by the Met Office Hadley Centre on a $5° \times 5°$ grid. HadSST4 quality controls and corrects biases in the in situ measurements from ICOADS 3.0.0 (1850–2014) and ICOADS 3.0.1 (2014–present), the central database of ship records (Freeman et al. 2017). HadSST4 provides non-infilled data as monthly means from 1850–present, and ship coverage varies substantially over time (Figure 1). Measurement and sampling errors are provided for every gridcell and month with data, and error covariance matrices are provided that estimate the spatially correlated errors. We include these sources of error in $\mathbf{R}$. Temporally correlated errors from uncertain bias corrections are estimated with a 200-member ensemble of observations, and we account for these errors with our ensemble DA method, described in Section 2b.

Observations of near-surface air temperature (T) over land are from CRUTEM5 version 5.0.2.0 (Osborn et al. 2021). Weather-station data is quality controlled, bias-corrected, and provided as monthly means with error estimates on a $5° \times 5°$ grid. We include CRUTEM5's time-varying measurement and sampling errors in $\mathbf{R}$.

Marine SLP observations are from ICOADS Enhanced Release 3.1 for 1850–2014 and Release 3.0.2, for 2015–2023 (Freeman et al. 2017). SLP data are provided as monthly means on a $2° \times 2°$ grid, along with the number of observations, n_{obs}, in each month and the intra-month standard deviation, s, of the observations in each gridcell. The baseline climatology for anomalies is provided by Hersbach et al. (2020). There are a large number of SLP observations due to the finer grid of ICOADS compared to HadSST4. We only assimilate gridcells with $n_{\text{obs}} \geq 5$, and for months that have data in more than 3000 gridcells, we mask up to 40% of the values between 25°S and 60°N using random sampling. Past studies identified a bias in ICOADS SLP data before 1870, which is discussed in Slivinski et al. (2019), Freeman et al. (2017), and Allan and Ansell (2006). NOAA 20CRv3 performed a bias correction of the pre-1870 SLP observations, so we substitute the 1850–1870 SLP from ICOADS with the collocated values from NOAA 20CRv3. ICOADS does not provide an estimate of measurement and sampling errors which comprise the diagonal terms in **R**, so we estimate **R** as described below.

To estimate **R** for the monthly mean SLP, we apply a method similar to that in Kaplan et al. (2000). The concept is that intramonth s, which is caused by submonthly variability, measurement error, and representativeness error, provides an estimate of the error in the monthly mean (Leith 1973). We take the local time-average of $s^2 \frac{n_{\text{obs}}}{n_{\text{obs}}-1}$ over the well observed period 1961–2023 to estimate the climatological error variance, σ^2, in the monthly mean for each gridcell, and we restrict the estimate to gridcells with $n_{\text{obs}} > 30$ in a given month. Again using a similar approach to Kaplan et al. (2000), we then spatially smooth the resulting climatological maps of σ using a running-mean window of 12° latitude × 50° longitude equatorward of 52°N/S and a window of 18° latitude × 100° longitude poleward of 52°N/S. This results in 12 monthly 2° × 2° fields of the random measurement and sampling error, σ_{random}.

We then must assign a time-varying error, σ, to each monthly value of SLP. We start with the random error described above, then reduce the random error by the number of intramonth observations in a gridcell. To account for autocovariance and possible sampling errors even when n_{obs} is large, reduce n_{obs} to $n_{\text{adjusted}} = n_{\text{obs}}/2$, and we set the maximum of n_{adjusted} at 30 (Leith 1973; Bretherton et al. 1999). We then consider the systematic component of the total error, $\sigma^2 = \sigma^2_{\text{systematic}} + \sigma^2_{\text{random}}/n_{\text{adjusted}}$, as discussed in Kennedy (2014). We estimate $\sigma^2_{\text{systematic}}$ from the variance across neighboring observations. The idea is that if neighboring observations consistently differ, the differences are from irreducible, systematic errors. Separately for each month from 1961–2023, we calculate the spatial variance across a running-mean window of 16° latitude × 32° longitude, restricting the calculation to gridcells with $n_{\text{obs}} \geq 5$. We use the zonal mean of the climatology of this field to represent $\sigma^2_{\text{systematic}}$. We make one adjustment by setting the minimum $\sigma_{\text{systematic}}$ at 6 hPa south of 72°S, preventing the error from getting small near Antarctica. The systematic error ranges from approximately 1 hPa on the equator to 7 hPa in polar regions, with a local maximum of 9.5 hPa over the Southern Ocean at 55°S.

Sea ice observations are provided by the NOAA/NSIDC Climate Data Record (CDR) of Passive Microwave Sea Ice Concentration, Version 4 from 11/1978–09/2023 and Near-Real-Time, Version 2, for 10/2023–12/2023 (Meier et al. 2021b,a). We coarsen the observations from 25 km to 2° resolution. At each timestep in the assimilation with satellite data, we use a subset of the available data, which includes nearly complete coverage of the polar regions. We retain all observations with SIC of 1%–98%, and we retain 40% of the remaining observations using random sampling. For measurement and sampling errors that form the diagonal terms in **R**, we use the provided standard deviations of daily values, but we set the minimum value to 1 percentage point. As previously described for SLP, these intramonth standard deviations approximate the monthly mean error and are calculated using both the NASA Team and Bootstrap algorithms, thereby estimating systematic error across data-processing methods. Errors are small in open water and pack ice but are often between 30 and 50 percentage points in partial ice cover. We do not have CDR data for sea ice from 1961–1978, but we need a full climatology from 1961–1990 to calculate the SIC anomalies relative to a baseline that is consistent with the HadSST4 anomalies. For 1/1961–11/1978, we use the multi-model mean of the historical simulations from the eight models used for LIM training, and use the merged climatology from 1961–1990 as the reference for SIC anomalies.

d. Validation: Pseudo-reconstruction of an out-of-sample model

To test our method, we mimic the real reconstruction problem and attempt to reconstruct the 1850–2014 historical simulation from a climate model. Our target model is MPI-ESM1-2-HR, ensemble member r1i1p1f1 (Mauritsen et al. 2019), and we have chosen MPI-ESM1-2-HR because it is a difficult test of the method. Unlike nearly all other models, it has cooling in the Southern Ocean from 1980–2014. It also has a low-bias in Antarctic sea ice (Roach et al. 2020), and substantially different ENSO statistics and radiative feedbacks (Bloch-Johnson et al. 2024) compared to the models used for LIMS and priors in the data assimilation. The pseudo-reconstruction's target is out-of-sample because MPI-ESM1-2-HR is not used for LIM training. The dynamics of the target model are unknown to our forecast models.

We draw pseudo-observations from the target simulation at the same times and locations where real observations are available for SST, T, SLP, and SIC. Random errors are added to the pseudo-observations by sampling from the real observation errors in **R**. Note that real observations also have biases and unknown, unquantified errors which make the real reconstruction more challenging than this test. On the other hand, the LIMs used as model priors are selected based on their ability to collectively emulate reality rather than the target model of the pseudo-reconstruction.

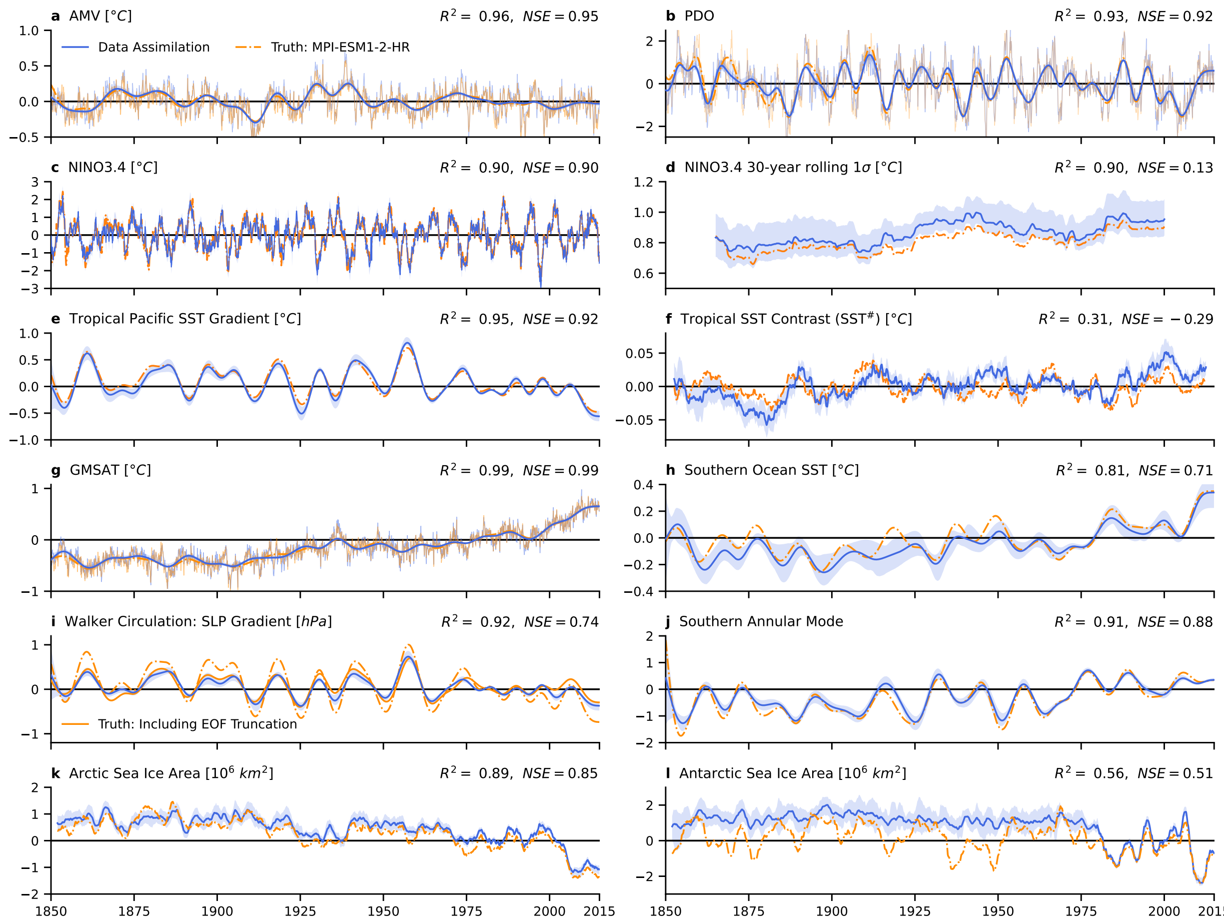

FIG. 2. **Validation by pseudo-reconstruction: variability timeseries.** (Orange) True values from the target model, the 1850–2014 historical simulation from MPI-ESM1-2-HR. (Blue) Result from data assimilation, showing mean of 1600 ensemble members; shading denotes ensemble 17$^{\text{th}}$ and 83$^{\text{rd}}$ percentiles, i.e., *likely* range. **(a)** Atlantic Multidecadal Variability with 10-yr low-pass filter and monthly values as thin lines. **(b)** Pacific Decadal Oscillation with 6-yr low-pass filter and monthly values as thin lines. **(c)** Monthly Nino3.4 with 30-yr running mean removed. **(d)** Rolling 30-yr standard deviation of Nino3.4 in panel **c**. **(e)** Zonal gradient of tropical Pacific SST with 10-yr low-pass filter. **(f)** Tropical SST contrast, SST$^{\#}$, 5-yr running mean. **(g)** Global-mean near-surface air temperature (GMSAT) with 10-yr low-pass filter and monthly values in thin lines. **(h)** Zonal mean of Southern Ocean SST (50°–70°S) with 10-yr low-pass filter. **(i)** Walker circulation, i.e., zonal SLP gradient across tropical Pacific, with 10-yr low-pass filter. **(j)** Southern Annular Mode with 10-yr low-pass filter. **(k)** Total area of Arctic sea ice with 24-month running mean. **(l)** Total area of Antarctic sea ice, with 24-month running mean. Calculation of metrics is described in Methods Section 2d.

Figure 2 shows timeseries representing climate variability from the pseudo-reconstruction. The ensemble mean is calculated as the grand mean across all 1600 ensemble members (8 LIMs × 200 members), and the ensemble shading spans the 17^{th}–83^{rd} percentiles. The various metrics in Figure 2 are calculated as follows, with anomalies representing the departures from the 1961–1990 climatological annual cycle unless stated otherwise:

- Atlantic multidecadal variability (AMV) is the monthly mean SST anomaly in the North Atlantic (0°–60°N, 80°W–0°W) minus the global mean; the mean of the index from 1900–1970 is removed before plotting (Trenberth and Shea 2006).
- The Pacific Decadal Oscillation (PDO) is the leading EOF of the monthly mean SST anomaly in the North Pacific (20°–70°N) after removing the global mean (Newman et al. 2016).
- Nino3.4 is the monthly mean SST anomaly from 170°W to 120°W and 5°S–5°N, with the 30-yr running mean removed.
- The zonal SST gradient in the tropical Pacific is the mean SST anomaly in the west (80°E–150°E) minus the east (160°W–80°W), spanning 5°S–5°N (Heede and Fedorov 2023).
- $SST^{\#}$, which denotes the tropical SST contrast, is the mean of the warmest 30% of tropical SSTs minus the tropical-mean SST, and the 1961–1990 mean is removed (Fueglistaler 2019).
- Southern Ocean SST is the zonal-mean SST anomaly from 50°–70°S (Doddridge and Marshall 2017).
- Global-mean near-surface air temperature (GMSAT) is the global-mean T anomaly.
- The Walker circulation, measured by the zonal SLP gradient, is the mean SLP anomaly in the west Pacific (130°E–150°E) minus the central-east Pacific (160°W–120°W), spanning 5°S–5°N (e.g., Heede and Fedorov 2023).
- The Southern Annular Mode (SAM) is the standardized zonal-mean SLP anomaly at 40°S ± 2° minus the standardized zonal-mean SLP anomaly at 65°S ± 2° (Gong and Wang 1999); the reference period for standardization is 1961–1990, and each month is standardized separately.
- Sea ice area is the sum of the products of SIC and gridcell area; note that a common land mask must be used when comparing ice area across datasets.

Most large-scale metrics are reconstructed with accuracy. We assess performance by the Pearson correlation (R), the fraction of variance explained (R^2) and the Nash-Sutcliffe Efficiency (NSE),

$$\mathrm{NSE} = 1 - \frac{\sum(x_i - \hat{x}_i)^2}{\sum(x_i - \bar{x})^2},$$

which accounts for the relative phasing of the true timeseries (x_i) versus the reconstructed timeseries ($\hat{x}_i$) the signal amplitude, and bias. The NSE has an upper bound equal to one and can become negative from bias in the mean or amplitude of variability (Nash and Sutcliffe 1970). We find $R^2 > 80\%$ for the AMV, PDO, Nino3.4, the 30-year rolling 1σ of Nino3.4, the zonal SST gradient in the tropical Pacific, GMSAT, Southern Ocean SST, the Walker circulation (zonal SLP gradient), the SAM, and Arctic ice area. The tropical SST contrast, $SST^{\#}$, is particularly difficult with the lowest $R^2 = 0.31$. NSE values are also shown in Figure 2.

The reconstruction of the Walker circulation has a damped amplitude compared to the target, which is due to the EOF truncation of SLP in the LIM training. We show an additional version of the target model's Walker circulation, which is calculated after truncating the target's SLP into the leading 30 EOFs. Truncation has a notable impact on tropical SLP because the variance in equatorial SLP is much smaller than the variance at higher latitudes, but truncation does not appear to have a substantial influence on other metrics.

Antarctic sea ice has $R^2 = 0.56$ and is biased high in the reconstruction pre-1979. The reason for this bias is that the target model is biased low relative to the multi-model mean of the LIMs and relative to the satellite record (Roach et al. 2020). There are decadal periods of abrupt ice loss in the target model which are not captured in the reconstruction. These ice-loss events are associated with brief warming episodes in Southern Ocean SST (Figure 2h), which are also not detected in the reconstruction. While we do not know whether such ice-loss events happen in nature, it is worth noting that if they do occur, our method cannot identify them in the sparse instrumental observations. Despite missing these decadal warmings, the lower-frequency variability in Southern Ocean SST and the SAM is captured by the reconstruction.

Figure 3 shows the pattern of trends in annual-mean SST for 1900–1979 and 1980–2014. Local trends are divided by the global-mean trend to emphasize the patterns, which are important for radiative feedbacks. We also show the reconstruction's ensemble spread (1σ) in trend patterns, which highlights regions of elevated uncertainty. It is important to recall that observations in the

Southern Ocean and southeast Pacific are sparse even after 1980 (Figure 1c), which is evident in our uncertainty quantification.

To further illustrate the uncertainty, we show trends from individual ensemble members (Figure 3c,g). These ensemble members show more cooling in the Southern Ocean than is seen in the ensemble mean. The takeaway message, which is relevant to the next section on the real reconstruction, is that our DA framework is capable of reconstructing cooling over the Southern Ocean, even though the models used to train the LIMs do not show post-1980 cooling over the Southern Ocean in their historical simulations.

Figure 4 shows trends in annual-mean SLP for 1900–1979 and 1980–2014. We only assimilate marine observations, hence terrestrial SLP is expected to deviate from the truth. Large-scale patterns are consistent, but the errors in the magnitude of trends are substantial, especially over the Southern Ocean. Sparse observations and the unique physics of the target model compared to the forecast models results in considerable uncertainty.

For additional validation, we show the spatial distribution of correlation and NSE in Supplemental Figures S1–S2. In Supplemental Figures S3–S4, we also show the correlation and NSE when using only one LIM instead of the multi-model mean of eight LIMs, which illustrates the major improvements from using multiple models in the reconstruction (Amrhein et al. 2020; Parsons et al. 2021). As a separate form of validation that does not involve pseudo-reconstruction, we evaluated the Desroziers statistics of the DA system (Desroziers et al. 2005). These results are shown in Supplemental Figure S5 and illustrate the calibration of the DA system.

e. Comparison data

We include a variety of datasets for comparison with our reconstruction. For SST, we focus on datasets which are globally complete and have monthly resolution. We include PCMDI/AMIPII (Hurrell et al. 2008), which was used for CMIP6's AMIP simulations, NOAA ERSSTv5 (Huang et al. 2017), HadISST1 (Rayner et al. 2003), HadISST2.1 (no longer maintained) (Titchner and Rayner 2014), and COBE-SST2 (Hirahara et al. 2014). The statistical infilling in these products is briefly described by Modak and Mauritsen (2023) and Lewis and Mauritsen (2021) and with more detail in Kent and Kennedy (2021). All products are regridded to the 2° resolution of our reconstruction.

For SLP, we show reanalyses from ERA5 (1949–present) from Hersbach et al. (2020), NOAA/CIRES/DOE 20CRv3 (1836–2015) from Slivinski et al. (2019), and NCEP/NCAR (1948–present) from Kalnay et al. (1996), all regridded to 2° and monthly resolution. We also include an older product, HadSLP2 (Allan and Ansell 2006). HadSLP2 is no longer maintained, but it provides monthly means of SLP and would be a companion to HadSST4 if updated. We include a proxy-based reconstruction of the Walker circulation from Falster et al. (2023), labeled F23, which used offline DA of proxies. We include the SAM from multiple reconstructions using offline DA (O'Connor et al. 2021; Dalaiden et al. 2021; King et al. 2023) and regression (Fogt et al. 2009), labeled as O21, D21, K23, and F09.

For SIC, we show HadISST2.2 (Titchner and Rayner 2014), HadISST1 (Rayner et al. 2003), and AMIPII (Hurrell et al. 2008), which is largely based on HadISST1. The satellite record from NOAA/NSIDC CDR (Meier et al. 2021b) is also shown from 11/1978–2023. We also include the proxy-based reconstruction of Arctic SIC from Brennan and Hakim (2022), labeled BH22, which has annual rather than monthly resolution. We regrid all SIC data to 2° resolution. When comparing total anomalies in Arctic ice area across datasets, we use a land mask that is common across all datasets. Otherwise, one dataset may have large anomalies where another dataset has missing values, skewing the comparison.

For global-mean T (GMSAT), we compare with HadCRUT5 and BEST (Morice et al. 2021; Rohde et al. 2013). Note that our reconstruction is of the near-surface air temperature, while the comparison datasets are hybrids of air temperature over land and SST over ocean.

Importantly, various instrumental datasets often impact one another. The lower boundary condition in ERA5 is the SST from HadISST2 until 2007 and sea ice from HadISST2 until 1979 (Hersbach et al. 2020). NOAA 20CRv3 also uses HadISST2 sea ice as a boundary condition from 1836–2015 and HadISST2 SST pre-1981 (Slivinski et al. 2019). The SST dataset ERSSTv5 uses the sea ice from HadISST2 to adjust its SST values in the Southern Ocean (Huang et al. 2017). These are examples of how uncertainty in one dataset might affect others.

3. Historical Reconstruction

In this section, we share the reconstruction of SST, T, SLP, and SIC from coupled atmosphere–ocean data assimilation with linear inverse models. We show timeseries of climate variability, spatial trends in SST, SLP, and SIC, and the El Niño beginning in 1877.

a. Variability from 1850–2023

Figure 5 shows variability timeseries, as described in the validation Figure 2. The AMV and PDO are similar across datasets for most of the historical record, as noted for the PDO in Newman et al. (2016), but there are substantial PDO differences from 1850–1900.

Nino3.4 shows substantial inter-dataset spread before 1875, but the most interesting ENSO feature is the low-frequency evolution of ENSO variance in Figure 5d, measured by the 30-year rolling 1σ of Nino3.4. Recent studies have argued for increased ENSO variance with global warming (e.g., Cai et al. 2021, 2023), although ENSO variance could decrease with long-term warming (Callahan et al. 2021). In our results, ENSO variance was at local maximum between 1875 and 1900 and at a local minimum 1930–1960. Figure 5d suggests considerable low-frequency fluctuations in ENSO variance, and it would be interesting to know whether there is a physical explanation for this time-evolution and muted ENSO variance in the mid-1900s.

Tropical SST gradients tell two different stories (Figure 5e,f). Recent trends from 1980–2023 in the zonal SST gradient (Figure 5e) suggest a minor strengthening, but the trend does not appear anomalous relative to past variability. However, a more physically motivated metric (Fueglistaler 2019; Fueglistaler and Silvers 2021), namely the contrast between the warmest tropical SSTs and the tropical mean SST ($SST^{\#}$ in Figure 5f), shows a prolonged strengthening from 1975–present. The 1975–2023 trend in $SST^{\#}$ may indeed be unique compared to the variability before 1975, but further investigation is needed.

The Walker circulation (zonal SLP gradient) appears consistent with natural variability over the full historical record (Figure 5i). Our reconstruction does not show a notable weakening of the Walker circulation over the 20th century (Vecchi et al. 2006; Tokinaga et al. 2012), nor does it display a notable recent strengthening since 1979 (Chung et al. 2019; L'Heureux et al. 2013; Watanabe et al. 2023). Heede and Fedorov (2023) found unique recent changes in the zonal SLP gradient using the NCEP/NCAR Reanalysis, but that product may be an outlier from 2005–2015

(Figure 5i). Watanabe et al. (2024) highlight trends since 1979 in multiple reanalyses, but those trends now seem less unique in light of the variability spanning 1850–2023.

Reconstruction of the Southern Annular Mode (SAM) is relatively confident based on our ensemble spread (Figure 5j). However, the pre-1980 disagreement across reanalyses and other reconstructions is substantial, and spurious trends have been identified in reanalyses poleward of 60°S (Fogt and Connolly 2021). Studies have highlighted the positive trend in the SAM from 1980–present (Marshall 2003; Swart et al. 2015; Banerjee et al. 2020), but some datasets in Figure 5j show longer-term positive trends, possibly spanning the entire 20$^{\text{th}}$ century (O'Connor et al. 2021). Our results indicate that the recent trend only extends from approximately 1975–present. There appears to be another prolonged positive trend from 1850–1920 in our reconstruction but not in any of the comparison data, and that SAM trend aligns with SST cooling in the Southern Ocean over the same period. Brönnimann et al. (2024) analyzed newly digitized ship records from 1903–1916 and also find the early 1900s to have a positive SAM and pronounced surface cooling over the Southern Ocean.

Sea ice has major differences with the HadISST1 and AMIPII datasets that have been used to assess radiative feedbacks over the historical record (Figure 5j,l). Over much of the historical record, these datasets have had to use constant climatologies. There are also differences in the satellite era because of uncertainties in data processing and discontinuities in the satellite sources. For example, there are spurious high values in Antarctic sea ice from 2009–2011 in HadISST1 and AMIPII (Screen 2011), shown in Figure 5l.

In Arctic sea ice, the main difference across datasets relates to the early 20$^{\text{th}}$-century warming (Hegerl et al. 2018). HadISST1 and AMIPII do not have any signal of the early 20$^{\text{th}}$-century warming in ice area. Our reconstruction shows a loss of 0.5 ± 0.1 (1σ) million km^2 during the 1920s, measured by comparing the decadal means of the 1930s and 1910s. Note that this value should not be compared directly with other datasets unless the land masks are consistent. The Brennan and Hakim (2022) reconstruction of annual means uses only proxy data in offline DA and agrees with our results after averaging their MPI and CCSM4 model priors.

Antarctic sea ice is a unique result compared to existing estimates. In stark contrast to the datasets used for CMIP6/DECK/AMIP/CFMIP (Webb et al. 2017) and as boundary conditions in reanalyses (e.g., Slivinski et al. 2019; Hersbach et al. 2020), our reconstruction shows much less ice loss from preindustrial to present conditions. AMIPII, HadISST1, and HadISST2 are at the edge or outside of our likely range for the entire pre-1980 period. Note that HadISST2 is the ice boundary condition in ERA5 and NOAA 20CRv3 before 1979, and it is used to adjust the SST in NOAA ERSSTv5. The differences in sea ice between AMIPII and HadISST2 cause a difference in the shortwave clear-sky feedback of approximately 0.6 W m^{-2} K^{-1} (SI of Andrews et al. 2018), illustrating the importantance of constraining the preindustrial uncertainty in Antarctic sea ice.

In the early 20^{th} century, we find a wide envelope of uncertainty in Antarctic ice area that spans the range over the satellite record until 2022. There may be sea ice expansion in the early 1900s, consistent with Brönnimann et al. (2024), and a decline in ice area from 1965–1980 (Fan et al. 2014). The preindustrial ice area (1850–1900) does not appear clearly different from the present range until the ice loss of 2022–2023 (Roach and Meier 2024; Espinosa et al. 2024; Zhang and Li 2023; Turner et al. 2022). Our results for preindustrial ice area are consistent with Edinburgh and Day (2016)'s analysis of ship records from the Heroic Age (1897–1917), which found ice expansion in the Weddell Sea but comparable conditions to 1989–2014 in the other sectors.

Finally, we consider the Southern Ocean SST (zonal mean from 50°–70°S). We find an impressive spread in our ensemble pre-1950 and a more-impressive disagreement across SST datasets, which persists from 1850 to 2023. We note two interesting takeaways in Figure 5h. First, there appears to be a long-term warming trend from 1910–2023, which is approximately aligned with the 1910–present warming trend in GMSAT. This is surprising because we expect Southern Ocean warming to be delayed relative to global-mean warming (Armour et al. 2016). We are curious whether there is a physical explanation for the Southern Ocean cooling from 1880–1910. Brönnimann et al. (2024) find that this cooling is a real climatic phenomenon, not a data artifact. However, Sippel et al. (2024) suggest that biases in the bucket measurements of SST are responsible for a cold bias from 1910–1930. If SST-bucket biases were responsible for the cooling rather than a climatic signal, we would need to explain why the night-time marine air temperatures (Cornes et al. 2020) show the same cooling trajectory as the SST (Figure 1a of Sippel et al. 2024).

Second, we find a muted cooling of the Southern Ocean from 1980–2013, and slight warming from 1980–2023. The comparison datasets are typically outside of our likely range. Observations are still sparse from 1980–2023 (Figure 1) and the in situ sources change dramatically over that period, possibly introducing spurious trends from homogenizing different data sources (Kennedy et al. 2019; Kent and Kennedy 2021; Hausfather et al. 2017; Karl et al. 2015). We elaborate on Southern Ocean trends below and in the Discussion.

b. Trends in SST, SLP, and sea ice

Figure 6 shows SST trends separately for the gradual warming from 1900–1979 and the recent period of 1980–2023. We show our reconstruction and its uncertainty alongside comparison trends from NOAA ERSSTv5 and COBE-SST2. Despite similar global-mean trends from 1900–1979, there are substantial disagreements in the pattern of trends especially over the Southern Ocean and tropical Pacific. The post-1980 period is viewed as having small uncertainty due to observation density (Figure 1), but the inter-dataset disagreements in Figure 6e-g suggest there are nontrivial differences in large-scale SST gradients. The southeast Pacific and Southern Ocean regions, which have recently been highlighted for their outsized impact on global climate and radiative feedbacks, have the worst observation coverage (Figure 1). The uncertainty in our reconstruction (Figure 6h), however, is not consistent with the range of disagreement across the existing SST datasets.

Figure 7 shows SLP trends for 1900–1979 and 1980–2023 from our reconstruction and comparison datasets. Note that our reconstruction only assimilates marine SLP observations, so we expect it to differ substantially over land regions where no local pressure data is assimilated. From 1900–1979, there are many large-scale differences between our reconstruction, HadSLP2, and NOAA 20CRv3. The comparison datasets show strong negative trends in SLP over Antarctica and most of the Southern Ocean for both time periods. Laloyaux et al. (2018) highlight problems with the general circulation in the Southern Hemisphere in multiple reanalyses and how those problems create spurious climate signals. The key problem identified in ERA-20C was the observation error for pressure data, which was too small. This is why we ensure our SLP observation error is not too small, as described in the Methods Section 2c.

From 1980–2023, our SLP trends over the global oceans largely align with ERA5, albeit with weaker positive trends in the central and eastern Pacific (Figure 7e,f). ERA5 has a substantial trend of increasing global-mean SLP of 21.1 Pa per 44 years from 1980–2023, and removing this trend would increase agreement with our reconstruction. NCEP/NCAR has a substantial trend of the opposite sign, which is –18.7 Pa. Our reconstruction does not have comparable trends in global-mean SLP, with a trend of 3.8 Pa (Figure 7e) and similarly small trends from 1900–1979 and in the validation (Figure 4). Once again, our reconstruction highlights uncertainty over the Southern Ocean, especially the Amundsen Sea Low and the Atlantic sector.

Figure 8 shows trends in Arctic SIC from 1900–1978, during the early 20$^{\text{th}}$-century warming from 1920–1935, and for the recent loss from 1980–2023. We compare with HadISST2, which is the pre-satellite boundary condition used in ERA5 and NOAA 20CRv3, and with the NOAA/NSIDC satellite data that we assimilate. From 1900–1978, we find ice loss in the Barents Sea between Svalbard and Russia. From 1920–1935, we find ice loss around most of the Arctic, offset by some gains poleward of the Bering Strait. HadISST2 does not have this 1920–1935 ice loss. From 1980–2023, our ice loss looks very similar to the satellite record, but it does not match exactly because of uncertainty in the satellite data, the influence of non-SIC observations, and the particularities of our LIM and DA methods.

Figure 9 shows trends in Antarctic SIC from 1900–1978, during the 1960–1978 period of ice loss hypothesized by Fan et al. (2014), and from 1979–2023, a period with steady but small growth and then recent rapid loss (e.g., Stuecker et al. 2017). Our reconstruction of 1900–1978 shows some ice loss alongside the Southern Ocean SST warming, but we find a lesser magnitude and a different pattern compared to HadISST2. If sea ice has a relationship with the atmospheric circulation (Kohyama and Hartmann 2016), the HadISST2 boundary condition may impact the circulation in ERA5 and NOAA 20CRv3. From 1960–1979, we find ice loss in the Atlantic sector, which mostly aligns with the pattern in HadISST2 but with a substantially different magnitude. We see a minor gain of ice in the Bellingshausen Sea, where HadISST2 shows large loss.

c. El Niño in 1877

The extreme El Niño that began in 1877, which is the largest event in the historical record, is an instructive comparison case for infilled datasets. Observations are sparse but the signal is large. Recent reconstructions of hybrid air/sea-surface temperature also focused on this event (Vaccaro et al. 2021; Kadow et al. 2020) to illustrate how different the imputed values can be for different datasets.

Figure 10 shows the onset of El Niño in July 1877. We show the ensemble spread in our reconstructed SST, the observations of SST and station temperatures, and two comparison datasets. ERSSTv5 depicts the center of action in the coastal eastern Pacific, whereas the central Pacific is most notable in HadISST1. Our ensemble mean displays some commonalities with each dataset and illustrates the large uncertainties in the central and coastal-eastern Pacific (Fig 10a). There are large differences in the North Pacific across the three results. Note that our reconstruction assimilates the land temperatures and SLP observations to inform the SST. In ERSSTv5, the influence of the HadISST2 sea ice is evident in the ring of cold anomalies around the Southern Ocean. This results from the expansion of Antarctic sea ice in HadISST2 (Figure 5l).

4. Discussion

a. Forced and internal variability

With a fresh look at the historical record, we could consider revisiting assessments of forced versus internal variability and trends. Recent studies have characterized the post-1980 changes in the tropical Pacific SST and Walker circulation (e.g., Watanabe et al. 2024), but placing those changes in the context of the full historical record may help disentangle the mechanisms of variability and determine drivers of trends and whether they are distinguishable from natural variability.

For example, it has been challenging to confirm whether the positive trend in the SAM (c. 1980–present) is caused by stratospheric ozone depletion, CO_2 forcing, natural variability, or other factors (Doddridge and Marshall 2017; Polvani et al. 2021; Bitz and Polvani 2012; Seviour et al. 2016; Thomas et al. 2015; Thompson et al. 2011; England et al. 2016; Fogt and Marshall 2020; Banerjee et al. 2020). These efforts have been complicated by results showing that the SAM has been trending positive over the entire twentieth century (Figure 5j). Our findings, which show no trend from 1925–1970, then a prolonged positive trend from 1970–present, may help determine drivers of the trend.

b. Climate model biases

Climate models have biases and are far from perfect. However, our reconstruction suggests that we could re-evaluate some of those large-scale biases. When considering joint analysis of SLP, SST, and/or sea ice (e.g., Wills et al. 2022; **?**; Dong et al. 2023; Purich et al. 2016; Kang et al. 2024), it would be ideal to compare models with reanalyses that use coupled data assimilation, ensuring that the SST and SLP are consistent with each other and with observations from both sources.

Unfortunately, other coupled instrumental reanalyses do not exist. In that case, we must carefully consider what the SST and SIC boundary conditions are that drive the atmospheric reanalyses. For example, ERA5 does not use the SST from NOAA ERSSTv5, it uses HadISST2 through August 2007 then switches to OSTIA (Donlon et al. 2012). When observations are sparse, the choice of SST and SIC used in the reanalysis may play a nontrivial role in trends on climate timescales.

In many cases, it is hard to know whether climate models cannot reproduce the relationships seen in certain observational datasets because (i) the climate models are wrong or (ii) we are inspecting relationships between SST/SIC products and reanalyses that used different SST/SIC products as their lower boundary conditions. This may not seem like an issue when looking at global or zonal means. But when investigating regional-scale coupled interactions between winds and SST, the observational uncertainties may be important. This consideration seems most likely to affect analyses of Southern Ocean SST, SAM, and Antarctic sea ice, and it may be impactful for the southeast and tropical Pacific.

We must not forget that infilled SST datasets, including the reconstruction produced in this study, are an uncertain representation of nature. For example, the southeast Pacific and the Southern Ocean (southeast-Pacific sector) appear to be prominent regions of systematic bias in SST and SLP in CMIP6 models from 1979–2022 (Wills et al. 2022), but these regions have sparse observation coverage (Figure 1c) and major changes in data sources from 1980–2023 (Kennedy et al. 2019). The Southern Ocean cooling post-1980 has been especially difficult for climate models to capture, and it plays an outsized role in global climate and radiative feedbacks (Kang et al. 2023b,a).

c. Southern Ocean cooling

Studies of Southern Ocean cooling typically use SSTs from NOAA ERSST, the latest of which is Version 5 (Huang et al. 2017). Even when nudging a climate model (CESM1) to the winds in ERA reanalysis, the climate model cannot reproduce the Southern Ocean SST cooling from ERSST (Blanchard-Wrigglesworth et al. 2021; Dong et al. 2022). Therefore, it seems that the winds cannot explain the SST cooling over the Southern Ocean (Dong et al. 2023).

Pacemaker experiments, which nudge a coupled climate model's SST in the Southern Ocean to match an infilled SST dataset (typically NOAA ERSST), have been used to investigate how SST cooling of the Southern Ocean affects global climate, radiative feedbacks, and the atmospheric circulation Zhang et al. (2021); Kang et al. (2024, 2023b,a). The Southern Ocean cooling has also been proposed as a driver of cooling in the tropical east Pacific (Dong et al. 2022), possibly forced by the ozone hole (Hartmann 2022) or other means (Watanabe et al. 2024). Kang et al. (2024) leverage the pacemaker experiments, and they highlight the importance of regional-scale discrepancies in SST trends for the atmospheric circulation and uncertainty in post-1979 trends across reanalyses in the Southern Hemisphere.

In our results, we find much less cooling over the Southern Ocean compared to NOAA ERSSTv5. However, it is possible that ERSSTv5 has the correct trend and our results are wrong. While more work is needed before conclusions can be made, we first compare the non-infilled SST dataset that we use to inform our data assimilation, HadSST4, with the non-infilled SST data from ERSSTv5 and from a recent product that has undergone extensive bias corrections (Chan et al. 2024). Then we compare with trends in other infilled SST datasets.

Figure 11a compares the non-infilled anomalies in the same southeast-Pacific sector of the Southern Ocean. We use the non-infilled data from ERSSTv5 and compare with DCENT (Chan et al. 2024) and HadSST4 (Kennedy et al. 2019), which are both non-infilled datasets. HadSST4 is used for our reconstruction. HadSST4 and DCENT show similar trajectories, but they have a substantial offsets relative to ERSSTv5. The idea is that not only the infilling but also the homogenization of time-varying data sources affects trends in this region. Kennedy et al. (2019) show the transition from bucket measurements to drifting buoys between 1980 and 2005, and Huang et al. (2019) find substantial differences in SST analyses from 2000–2016 when including drifting buoy and/or ARGO floats in NOAA ERSSTv5. ERSSTv5 has undergone extensive bias corrections and investigation of uncertainty, so the ERSSTv5 analysis may be correct in this region. The key point is that the handling of time-varying data sources may have a large influence on what initially appear to be climate trends. We hope our results motivate future efforts to refine SST data from the Southern Ocean.

Figure 11b shows the distribution of 1980–2023 SST trends in the southeast-Pacific sector of the Southern Ocean (ADD lat-lon range). Our reconstruction shows a wide range of uncertainty, with possible trends ranging from –0.3°C to 0.0°C (44 yr)$^{-1}$. Our distribution is shaped by the uncertainty in bias corrections from HadSST4 and by the eight LIMs used as priors in the assimilation. COBE-SST2 and HadISST1 are within our uncertainty range, but ERSSTv5 has a larger trend of –0.7°C (44 yr)$^{-1}$. Determining which of these trends is correct seems important to advancing understanding of the mechanisms driving Southern Ocean cooling. For example, nudging a climate model's winds to reanalysis may not explain the cooling in ERSSTv5, but maybe wind-nudging could explain the cooling in our reconstruction. If our reconstruction is correct, we could consider revisiting the investigations of Southern Ocean cooling, its impacts on the tropical Pacific and global climate, and the related criticisms of climate models.

d. Future opportunities and caveats of the method

Future efforts to reconstruct the historical record could improve on our results in a variety of ways, and we list a few of them here:

- LIMs and DA: Future investigations could elaborate on optimizing the LIMs, their training data, and possibly consider machine-learning methods (e.g., Meng and Hakim 2024). Our method uses climate models to train the LIMs, and therefore inherits some of the problems in climate models. We mitigate this effect by using eight different CMIP6 models and with DA. There are many different varieties of DA that could be tested, including 4D-Var, quantile-conserving filtering, or multi-model Kalman filtering (Kalnay 2003; Houtekamer and Zhang 2016; Anderson 2022; Bach and Ghil 2023). Our method assumes state variables can be approximated with Gaussian distributions, which appears to work reasonably well for SIC but could likely be improved in future studies.

- Pressure data: HadSLP2 needs to be updated (Allan and Ansell 2006). A quality-controlled version of monthly mean SLP and error estimates, structured like those of HadSST4, would be helpful. ICOADS has an abundance of marine data (Freeman et al. 2017), but ICOADS data is not in an optimal form for climate reconstructions and does not include estimates of the observation error.

- Sea ice: There are many observations available before the satellite era (e.g., Walsh et al. 2019; Edinburgh and Day 2016; Titchner and Rayner 2014), but we do not have a current compilation of this data in a format that can be used in reconstructions. A dataset structured like HadSST4 or DCENT but with historical SIC observations would be immensely helpful.

- SST: Ongoing efforts to digitize new data, quantify error, and correct the biases of existing data will continue to be critical (e.g., Brönnimann et al. 2024; Chan et al. 2019, 2023; Kent and Kennedy 2021; Kennedy et al. 2019). For SST anomalies, it would be helpful to use a climatological period that overlaps with satellite observations of SIC (i.e., post-1979).

5. Conclusions

The historical record is essential to our understanding of coupled climate dynamics and variability, but observations are sparse and prone to error. In this study, we use coupled data assimilation to combine climate models and instrumental observations over the historical record. At monthly resolution on a global $2^\circ \times 2^\circ$ grid, we reconstruct SST, near-surface air temperature, sea-level pressure, and sea-ice concentration from 1850–2023, and we quantify the time-varying uncertainty in all fields and its spatial fingerprints. Our results include 1600 ensemble members of globally resolved SST and SIC at monthly resolution, which can be used as boundary conditions in atmospheric general circulation models (i.e., AMIP-type simulations).

The reconstruction is internally consistent across the atmosphere, ocean, and ice components, and observations from the various components inform the full state estimate in every month. We construct the prior for each month by forecasting from the previous month's posterior analysis, i.e., our method retains memory of past observations in the time-evolving state estimates. We account for model uncertainty by training linear inverse models on eight different CMIP6 models, which are used to forecast the prior. We account for observational uncertainty by using the Kalman filter and by propagating the uncertainty in bias corrections from HadSST4's 200-member ensemble of SST observations.

In many ways, our results differ from comparison datasets regarding how recent (c. 1980–present) trends compare to past variability. The recent evolution of the Walker circulation appears consistent with past variability, as does the zonal SST gradient in the tropical Pacific. However, the SST contrast ($SST^{\#}$) between the warmest regions and the rest of the Tropics, exhibits a prolonged strengthening from 1975–present that may be distinct from past variability.

In the Southern Ocean, we find a relatively muted cooling of SST from 1980–present. We highlight the observational uncertainty over the Southern Ocean, which merits more attention due to issues homogenizing data sources and imputing missing values even post-1980. The

Southern Annular Mode and Antarctic sea ice follow very different trajectories in our reconstruction compared to most estimates over the majority of the record (1850–1980). A key result is our constraints on Antarctic sea ice. We find much less ice loss from 1900–1980 compared to existing datasets but with large uncertainty.

The historical reconstruction is available for climate analysis and uncertainty quantification. We provide the grand-ensemble mean of all 1600 members, the separate ensemble means for each of the eight model priors, and a subset of 200 fully gridded ensemble members. This reconstruction provides a foundation for advancing our understanding of climate dynamics and historical variability, while also serving as a resource for evaluating climate models, assessing uncertainties, and guiding future investigations into coupled atmosphere–ocean–ice interactions.

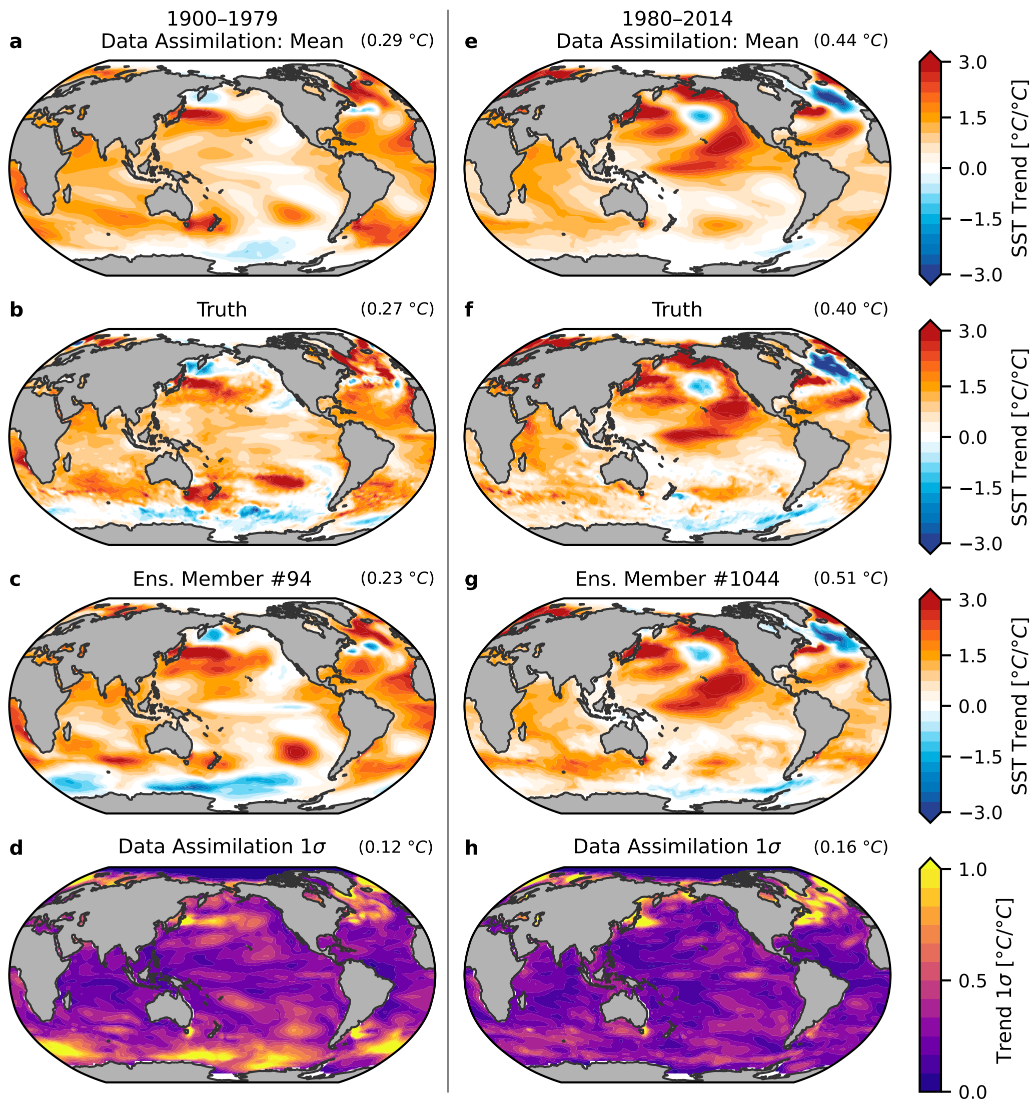

FIG. 3. **Validation by pseudo-reconstruction: SST trends.** **(a)** Normalized 1900–1979 ensemble mean of trends from data assimilation; local trends are divided by the global-mean trend to show SST patterns; upper-right indicates the global-mean trend before normalization, scaled by the number of years to show trend in °C per 80 years. **(b)** Repeats panel **a** but showing true trends in the pseudo-reconstruction's target model, MPI-ESM1-2-HR's historical simulation. **(c)** Repeats panel **a** but shows an individual member from ensemble data assimilation. **(d)** Uncertainty in results from data assimilation, calculated as the sample standard deviation (1σ) across 1600 ensemble members' normalized trends; values greater than 1.0 indicate that local 1σ is greater than the global-mean trend; upper-right shows the global-mean of the 1σ in local trends before normalization. **(e–f)** Repeats panels **a–d** for 1980–2014.

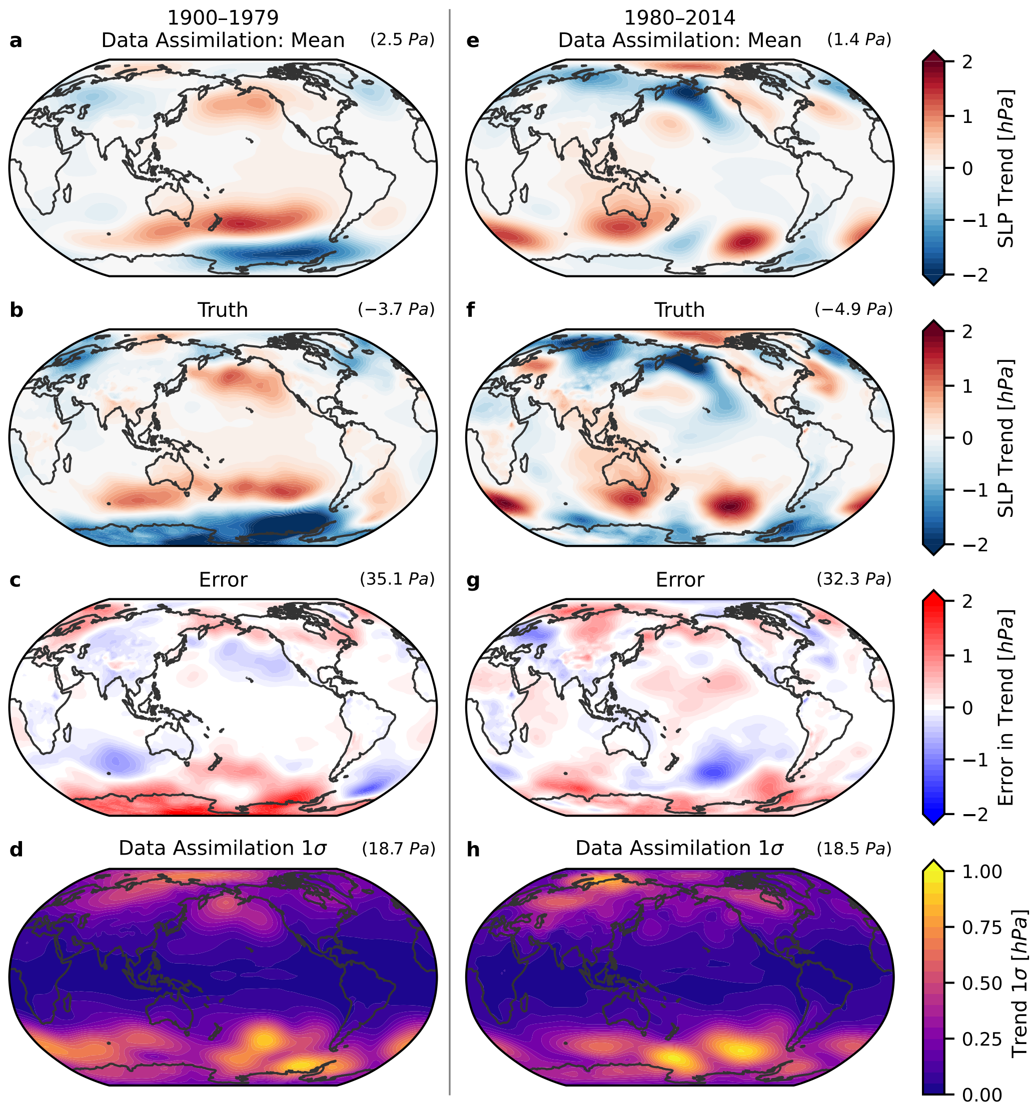

FIG. 4. **Validation by pseudo-reconstruction: trends in sea-level pressure (SLP). (a)** 1900–1979 ensemble mean of trends from data assimilation, scaled by the number of years to show trends in hPa per 80 years; upper-right indicates the global-mean trend in Pa per 80 years. **(b)** Repeats panel **a** but showing true trends in the pseudo-reconstruction's target model, MPI-ESM1-2-HR's historical simulation. **(c)** Error, shown as mean reconstruction minus truth; RMSE shown in upper right. **(d)** Uncertainty in results from data assimilation, calculated as the sample standard deviation (1σ) across trends from 1600 ensemble members; upper-right shows the global mean of the 1σ in local trends. **(e–f)** Repeats panels **a–d** for 1980–2014.

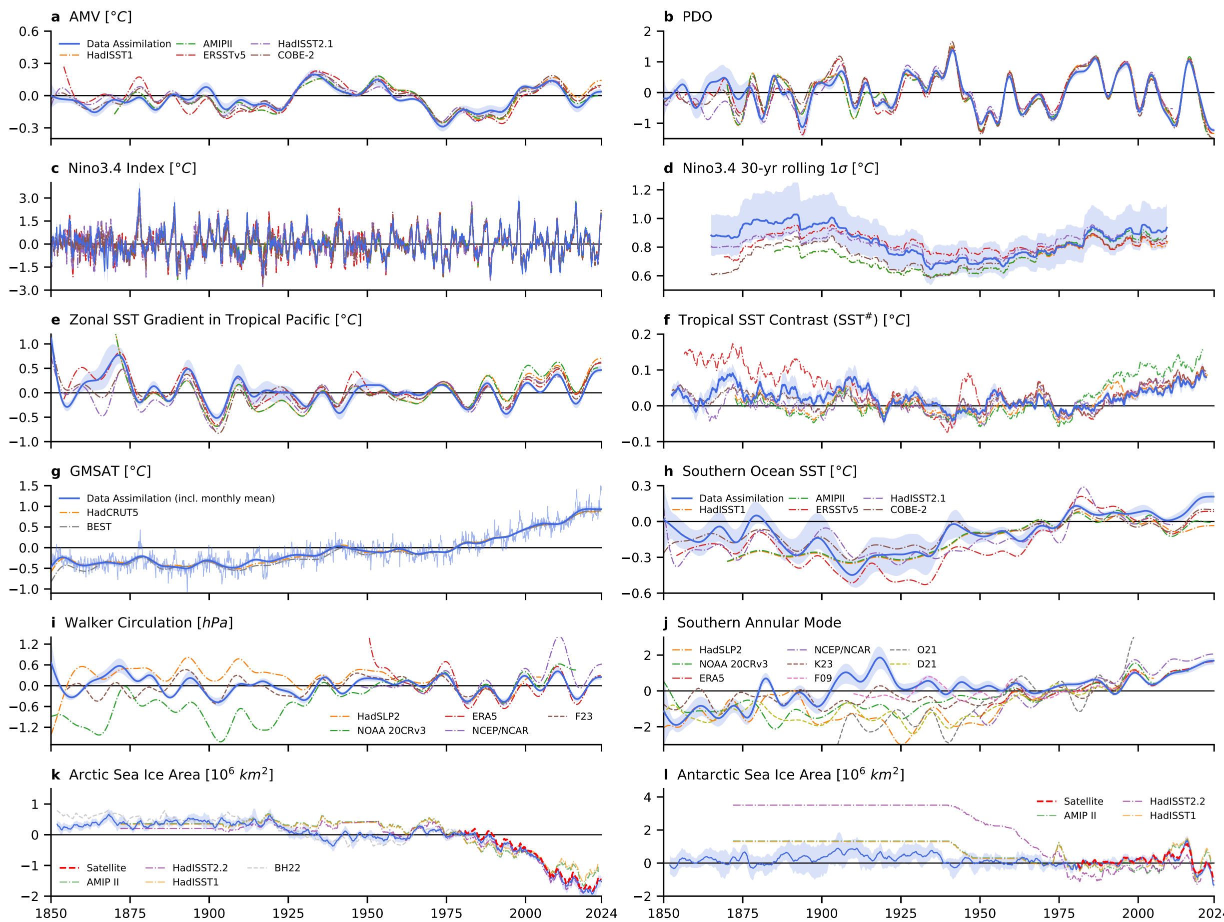

FIG. 5. **Climate variability from 1850–2023.** (Blue) Results from data assimilation, showing mean of 1600 ensemble members; shading denotes ensemble 17$^{\text{th}}$ and 83$^{\text{rd}}$ percentiles, i.e., *likely* range. Note that legend for SST datasets in panel **a** applies to panels **a–f**, and re-used line colors in SLP, T, and SIC panels do not necessarily indicate consistency with the SST datasets. **(a)** Atlantic Multidecadal Variability (SST) with 10-yr low-pass filter. **(b)** Pacific Decadal Oscillation (SST) with 6-yr low-pass filter. **(c)** Monthly SST in Nino3.4 region with 30-yr running mean removed. **(d)** Rolling 30-yr standard deviation of Nino3.4 in panel **c**. **(e)** Zonal gradient of tropical Pacific SST with 10-yr low-pass filter. **(f)** Tropical SST contrast, SST$^{\#}$, 5-yr running mean. **(g)** Global-mean near-surface air temperature (GMSAT) with 10-yr low-pass filter and monthly values from data assimilation as thin line. **(h)** Zonal mean of Southern Ocean SST (50°–70°S) with 10-yr low-pass filter. **(i)** Walker circulation, i.e., zonal SLP gradient across tropical Pacific, with 10-yr low-pass filter. **(j)** Southern Annular Mode (SLP) with 10-yr low-pass filter. **(k)** Total area of Arctic sea ice with 24-month running mean, with satellite data from NOAA/NSIDC CDR. **(l)** Total area of Antarctic sea ice, with 24-month running mean. Calculation of metrics is described in Methods Section 2d, and comparison data is summarized in Methods Section 2e.

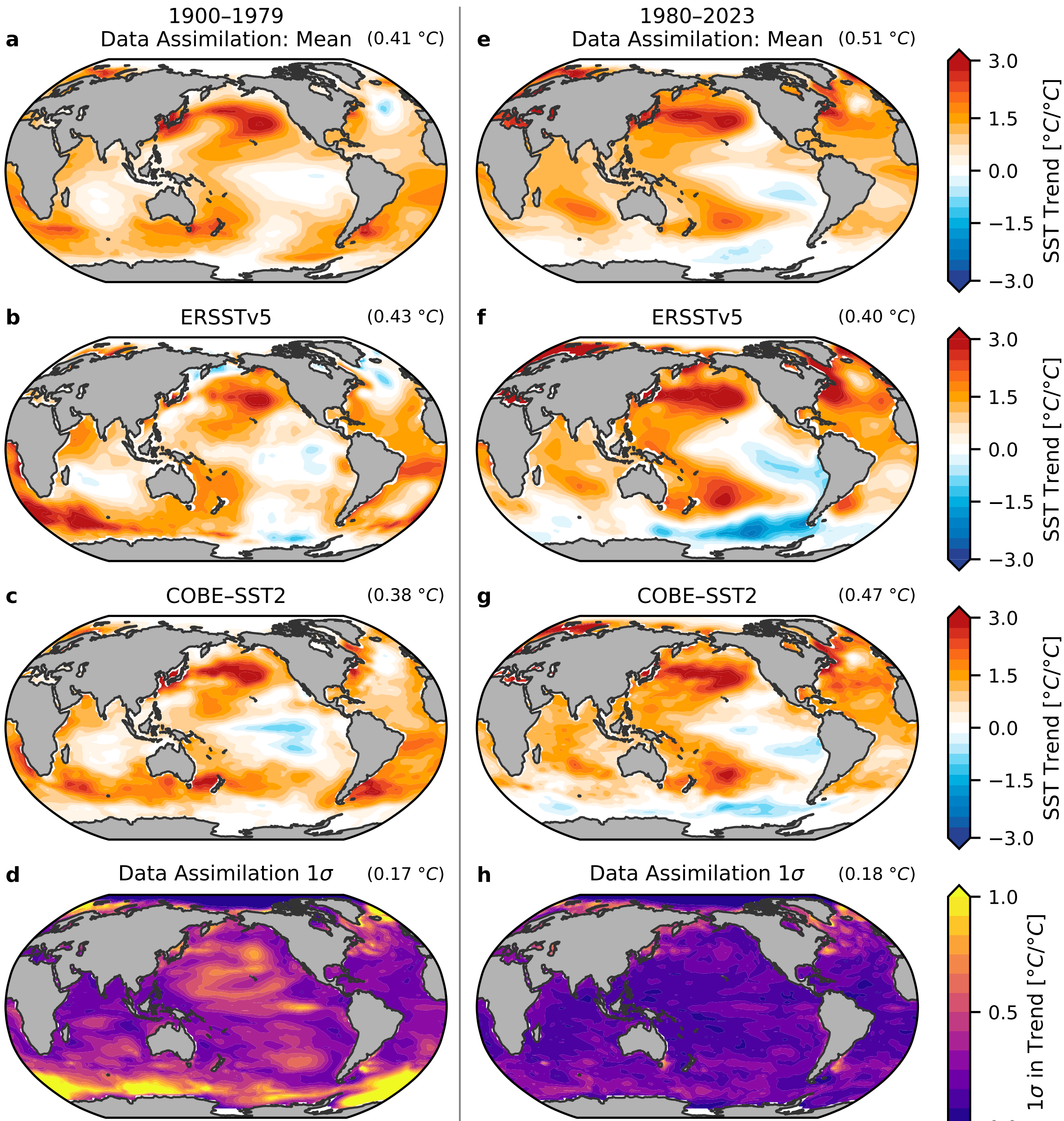

Fig. 6. **Historical patterns of SST trends.** **(a)** Normalized 1900–1979 ensemble mean of trends from data assimilation; local trends are divided by the global-mean trend to show SST patterns; upper-right indicates the global-mean trend before normalization, scaled by the number of years to show trend in °C per 80 years. **(b)** Repeats panel **a** but showing comparison data from NOAA ERSSTv5 and **(c)** COBE-SST2. **(d)** Uncertainty in results from data assimilation, calculated as the sample standard deviation (1σ) across 1600 ensemble members' normalized trends; values greater than 1.0 indicate that local 1σ is greater than the global-mean trend; upper-right shows the global-mean of the 1σ in local trends before normalization. **(e–f)** Repeats panels **a–d** for 1980–2023.

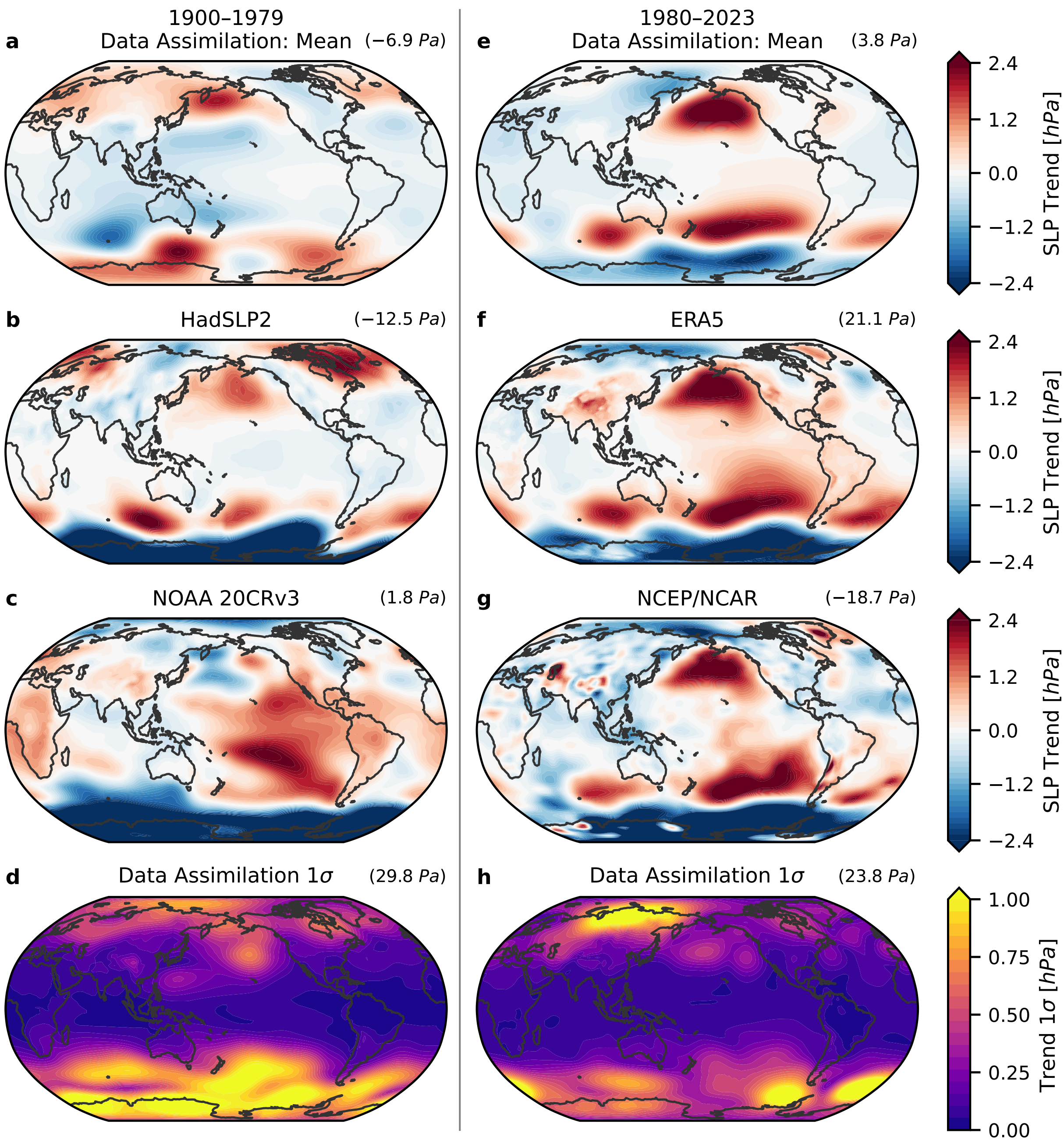

FIG. 7. **Historical trends in sea-level pressure (SLP). (a)** 1900–1979 ensemble mean of trends from data assimilation, scaled by the number of years to show trends in hPa per 80 years; upper-right indicates the global-mean trend in Pa per 80 years. **(b)** Repeats panel **a** but showing comparison datasets HadSLP2 and **(c)** NOAA 20CRv3. **(d)** Uncertainty in results from data assimilation, calculated as the sample standard deviation (1σ) across local trends from 1600 ensemble members; upper-right shows the global mean of the 1σ in local trends. **(e–f)** Repeats panels **a–d** for 1980–2023, with comparison reanalyses from **(f)** ERA5 and **(g)** NCEP/NCAR.

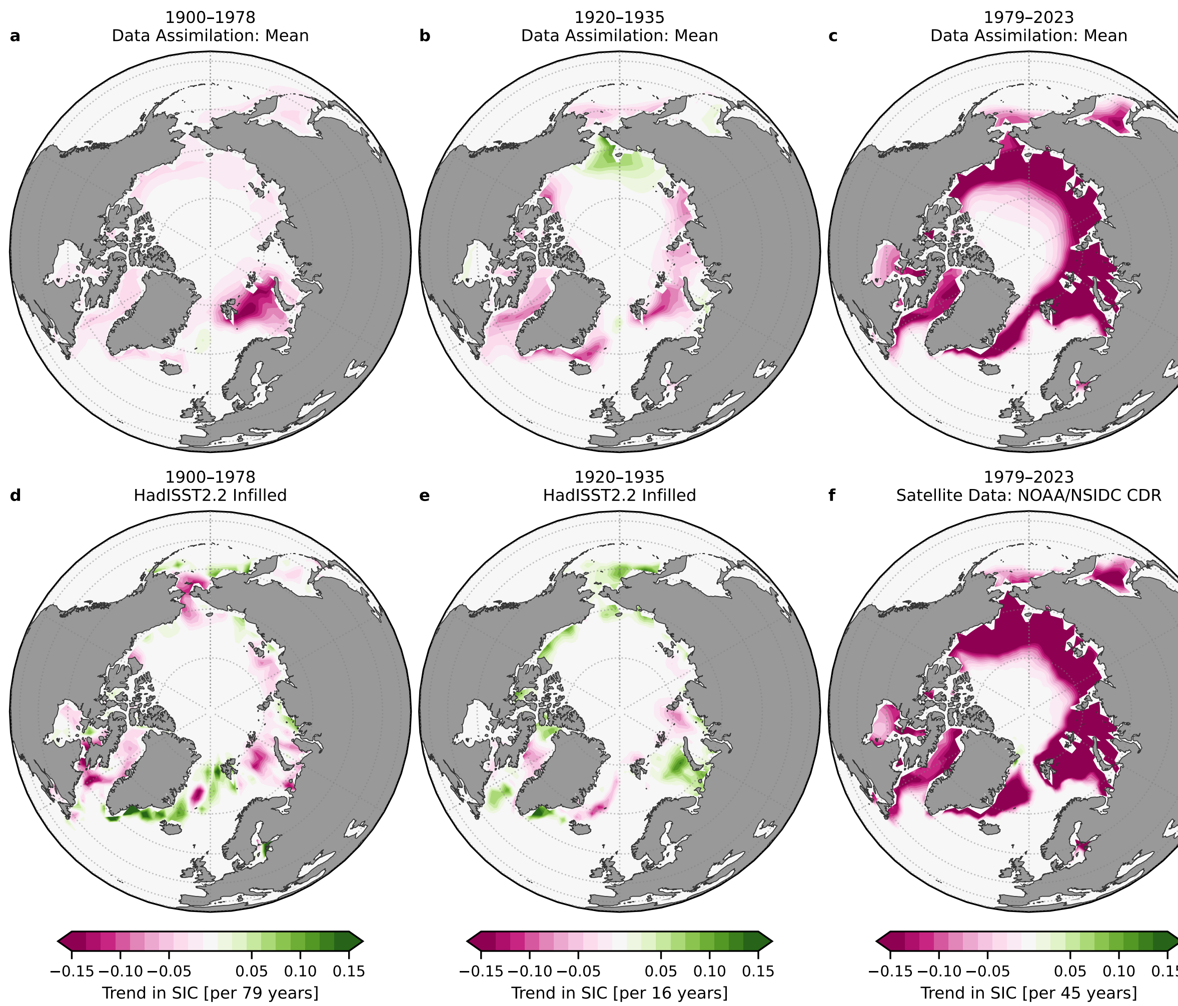

FIG. 8. **Historical trends in Arctic sea-ice concentration (SIC). (a–c)** Ensemble mean of trends from data assimilation, scaled by the number of years in each time period to show trends in SIC per *N* years. **(d–f)** Repeats panels **a–c** but showing comparison datasets, with infilled HadISST2.2 in panels **d–e** and NOAA/NSIDC CDR from satellite data in panel **f**. Note that SIC is bounded from 0 to 1.

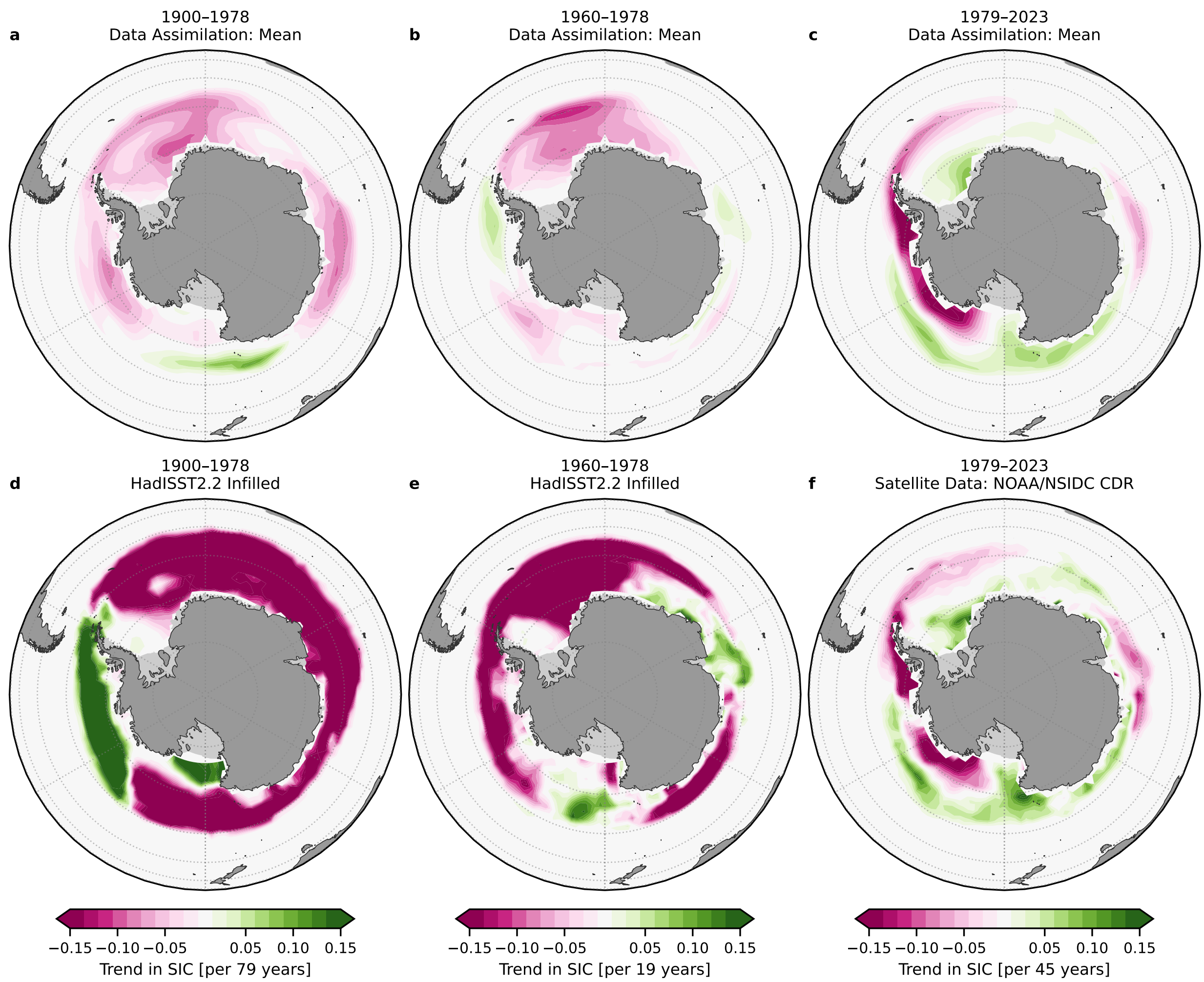

FIG. 9. **Historical trends in Antarctic sea-ice concentration (SIC). (a–c)** Ensemble mean of trends from data assimilation, scaled by the number of years in each time period to show trends in SIC per N years. **(d–f)** Repeats panels **a–c** but showing comparison datasets, with infilled HadISST2.2 in panels **d–e** and NOAA/NSIDC CDR from satellite data in panel **f**. Note that SIC is bounded from 0 to 1.

APPENDIX

Summary of Training Data for Linear Inverse Models

Model	Total Years (piControl range)	Ens. Mem.	EOFs	Reference
CESM2	1166 (200–1200)	r1i1p1f1	408	Danabasoglu et al. (2020)
UKESM1.0	1754 (2250–3839)	r1i1p1f2	408	Sellar et al. (2019)
SAM0-UNICON	865 1–700	r1i1p1f1	306	Park et al. (2019)
GFDL-ESM4	665 (1–500)	r1i1p1f1	306	Dunne et al. (2020)
NorESM2-LM	666 (1600–2100)	r1i1p1f1	306	Seland et al. (2020)
EC-Earth3	1165 (2103–3102)	r2i1p1f1	408	Döscher et al. (2022)
HadGEM3-GC31-LL	2165 (1850–3849)	r1i1p1f1	408	Kuhlbrodt et al. (2018)
E3SM-2	665 (1–500)	r1i1p1f1	306	Qin et al. (2024)

TABLE A1. CMIP6 training data for 8 linear inverse models. All models with 408 EOFs have the following distribution across state variables: 108 SST, 108 T, 48 SLP, 72 Arctic SIC, 72 Antarctic SIC. Models with 306 EOFs have 92 SST, 84 T, 30 SLP, 50 Arctic SIC, 50 Antarctic SIC. Note that Total Years includes piControl plus 165 years of historical simulation from 1850–2014.

References

Allan, R., and T. Ansell, 2006: A New Globally Complete Monthly Historical Gridded Mean Sea Level Pressure Dataset (HadSLP2): 1850–2004. *Journal of Climate*, **19 (22)**, 5816–5842, https://doi.org/10.1175/JCLI3937.1.

Amrhein, D. E., G. J. Hakim, and L. A. Parsons, 2020: Quantifying Structural Uncertainty in Paleoclimate Data Assimilation With an Application to the Last Millennium. *Geophysical Research Letters*, **47 (22)**, https://doi.org/10.1029/2020GL090485.

Anderson, J. L., 2022: A Quantile-Conserving Ensemble Filter Framework. Part I: Updating an Observed Variable. *Monthly Weather Review*, **150 (5)**, 1061–1074, https://doi.org/10.1175/MWR-D-21-0229.1.

Andrews, T., J. M. Gregory, and M. J. Webb, 2015: The Dependence of Radiative Forcing and Feedback on Evolving Patterns of Surface Temperature Change in Climate Models. *Journal of Climate*, **28 (4)**, 1630–1648, https://doi.org/10.1175/JCLI-D-14-00545.1.

Andrews, T., and M. J. Webb, 2018: The Dependence of Global Cloud and Lapse Rate Feedbacks on the Spatial Structure of Tropical Pacific Warming. *Journal of Climate*, **31 (2)**, 641–654, https://doi.org/10.1175/JCLI-D-17-0087.1.

Andrews, T., and Coauthors, 2018: Accounting for Changing Temperature Patterns Increases Historical Estimates of Climate Sensitivity. *Geophysical Research Letters*, **45 (16)**, 8490–8499, https://doi.org/10.1029/2018GL078887.

Andrews, T., and Coauthors, 2022: On the Effect of Historical SST Patterns on Radiative Feedback. *Journal of Geophysical Research: Atmospheres*, **127 (18)**, https://doi.org/10.1029/2022JD036675.

Armour, K. C., C. M. Bitz, and G. H. Roe, 2013: Time-Varying Climate Sensitivity from Regional Feedbacks. *Journal of Climate*, **26 (13)**, 4518–4534, https://doi.org/10.1175/JCLI-D-12-00544.1.

Armour, K. C., J. Marshall, J. R. Scott, A. Donohoe, and E. R. Newsom, 2016: Southern Ocean warming delayed by circumpolar upwelling and equatorward transport. *Nature Geoscience*, **9 (7)**, 549–554, https://doi.org/10.1038/ngeo2731.

Bach, E., and M. Ghil, 2023: A Multi-Model Ensemble Kalman Filter for Data Assimilation and Forecasting. *Journal of Advances in Modeling Earth Systems*, **15 (1)**, https://doi.org/10.1029/2022MS003123.

Banerjee, A., J. C. Fyfe, L. M. Polvani, D. Waugh, and K.-L. Chang, 2020: A pause in Southern Hemisphere circulation trends due to the Montreal Protocol. *Nature*, **579 (7800)**, 544–548, https://doi.org/10.1038/s41586-020-2120-4.

Battisti, D. S., D. J. Vimont, and B. P. Kirtman, 2019: 100 Years of Progress in Understanding the Dynamics of Coupled Atmosphere–Ocean Variability. *Meteorological Monographs*, **59**, 1–8, https://doi.org/10.1175/AMSMONOGRAPHS-D-18-0025.1.

Bitz, C. M., and L. M. Polvani, 2012: Antarctic climate response to stratospheric ozone depletion in a fine resolution ocean climate model. *Geophysical Research Letters*, **39 (20)**, https://doi.org/10.1029/2012GL053393.

Blanchard-Wrigglesworth, E., L. A. Roach, A. Donohoe, and Q. Ding, 2021: Impact of Winds and Southern Ocean SSTs on Antarctic Sea Ice Trends and Variability. *Journal of Climate*, **34 (3)**, 949–965, https://doi.org/10.1175/JCLI-D-20-0386.1.

Bloch-Johnson, J., and Coauthors, 2024: The Green's Function Model Intercomparison Project (GFMIP) Protocol. *Journal of Advances in Modeling Earth Systems*, **16 (2)**, https://doi.org/10.1029/2023MS003700.

Brennan, M. K., and G. J. Hakim, 2022: Reconstructing Arctic Sea Ice over the Common Era Using Data Assimilation. *Journal of Climate*, **35 (4)**, 1231–1247, https://doi.org/10.1175/JCLI-D-21-0099.1.

Brennan, M. K., G. J. Hakim, and E. Blanchard-Wrigglesworth, 2023: Monthly Arctic Sea-Ice Prediction With a Linear Inverse Model. *Geophysical Research Letters*, **50 (7)**, e2022GL101 656, https://doi.org/10.1029/2022GL101656.

Bretherton, C. S., M. Widmann, V. P. Dymnikov, J. M. Wallace, and I. Bladé, 1999: The effective number of spatial degrees of freedom of a time-varying field. *Journal of Climate*, https://doi.org/10.1175/1520-0442(1999)012⟨1990:TENOSD⟩2.0.CO;2.

Brönnimann, S., 2009: Early twentieth-century warming. *Nature Geoscience*, **2 (11)**, 735–736, https://doi.org/10.1038/ngeo670.

Brönnimann, S., Y. Brugnara, and C. Wilkinson, 2024: Early 20th century Southern Hemisphere cooling. *Climate of the Past*, **20 (3)**, 757–767, https://doi.org/10.5194/cp-20-757-2024.

Burgers, G., P. Jan van Leeuwen, and G. Evensen, 1998: Analysis Scheme in the Ensemble Kalman Filter. *Monthly Weather Review*, **126 (6)**, 1719–1724, https://doi.org/10.1175/1520-0493(1998)126⟨1719:ASITEK⟩2.0.CO;2.

Cai, W., and Coauthors, 2021: Changing El Niño–Southern Oscillation in a warming climate. *Nature Reviews Earth & Environment*, **2 (9)**, 628–644, https://doi.org/10.1038/s43017-021-00199-z.

Cai, W., and Coauthors, 2023: Anthropogenic impacts on twentieth-century ENSO variability changes. *Nature Reviews Earth & Environment*, **4 (6)**, 407–418, https://doi.org/10.1038/s43017-023-00427-8.

Callahan, C. W., C. Chen, M. Rugenstein, J. Bloch-Johnson, S. Yang, and E. J. Moyer, 2021: Robust decrease in El Niño/Southern Oscillation amplitude under long-term warming. *Nature Climate Change*, **11 (9)**, 752–757, https://doi.org/10.1038/s41558-021-01099-2.

Ceppi, P., and J. M. Gregory, 2017: Relationship of tropospheric stability to climate sensitivity and Earth's observed radiation budget. *Proceedings of the National Academy of Sciences*, **114 (50)**, 13 126–13 131, https://doi.org/10.1073/pnas.1714308114.

Chan, D., G. Gebbie, and P. Huybers, 2023: Global and Regional Discrepancies between Early-Twentieth-Century Coastal Air and Sea Surface Temperature Detected by a Coupled Energy-Balance Analysis. *Journal of Climate*, **36 (7)**, 2205–2220, https://doi.org/10.1175/JCLI-D-22-0569.1.

Chan, D., G. Gebbie, P. Huybers, and E. C. Kent, 2024: A Dynamically Consistent ENsemble of Temperature at the Earth surface since 1850 from the DCENT dataset. *Scientific Data*, **11 (1)**, 953, https://doi.org/10.1038/s41597-024-03742-x.

Chan, D., and P. Huybers, 2019: Systematic Differences in Bucket Sea Surface Temperature Measurements among Nations Identified Using a Linear-Mixed-Effect Method. *Journal of Climate*, **32 (9)**, 2569–2589, https://doi.org/10.1175/JCLI-D-18-0562.1.

Chan, D., E. C. Kent, D. I. Berry, and P. Huybers, 2019: Correcting datasets leads to more homogeneous early-twentieth-century sea surface warming. *Nature*, **571 (7765)**, 393–397, https://doi.org/10.1038/s41586-019-1349-2.

Chung, E.-S., A. Timmermann, B. J. Soden, K.-J. Ha, L. Shi, and V. O. John, 2019: Reconciling opposing Walker circulation trends in observations and model projections. *Nature Climate Change*, **9 (5)**, 405–412, https://doi.org/10.1038/s41558-019-0446-4.

Coats, S., and K. B. Karnauskas, 2017: Are Simulated and Observed Twentieth Century Tropical Pacific Sea Surface Temperature Trends Significant Relative to Internal Variability? *Geophysical Research Letters*, **44 (19)**, 9928–9937, https://doi.org/10.1002/2017GL074622.

Coats, S., J. E. Smerdon, S. Stevenson, J. T. Fasullo, B. Otto-Bliesner, and T. R. Ault, 2020: Paleoclimate Constraints on the Spatiotemporal Character of Past and Future Droughts. *Journal of Climate*, **33 (22)**, 9883–9903, https://doi.org/10.1175/JCLI-D-20-0004.1.

Compo, G. P., and Coauthors, 2011: The Twentieth Century Reanalysis Project. *Quarterly Journal of the Royal Meteorological Society*, **137 (654)**, 1–28, https://doi.org/10.1002/qj.776.

Cooper, V. T., and Coauthors, 2024: Last Glacial Maximum pattern effects reduce climate sensitivity estimates. *Science Advances*, **10 (16)**, 9461, https://doi.org/10.1126/sciadv.adk9461.

Cornes, R. C., E. Kent, D. Berry, and J. J. Kennedy, 2020: CLASSnmat: A global night marine air temperature data set, 1880–2019. *Geoscience Data Journal*, **7 (2)**, 170–184, https://doi.org/10.1002/gdj3.100.

Cowtan, K., and R. G. Way, 2014: Coverage bias in the HadCRUT4 temperature series and its impact on recent temperature trends. *Quarterly Journal of the Royal Meteorological Society*, **140 (683)**, https://doi.org/10.1002/qj.2297.

Dalaiden, Q., H. Goosse, J. Rezsöhazy, and E. R. Thomas, 2021: Reconstructing atmospheric circulation and sea-ice extent in the West Antarctic over the past 200 years using data assimilation. *Climate Dynamics*, **57 (11-12)**, 3479–3503, https://doi.org/10.1007/s00382-021-05879-6.

Danabasoglu, G., and Coauthors, 2020: The Community Earth System Model Version 2 (CESM2). *Journal of Advances in Modeling Earth Systems*, **12 (2)**, https://doi.org/10.1029/2019MS001916.

Deser, C., M. A. Alexander, S.-P. Xie, and A. S. Phillips, 2010: Sea Surface Temperature Variability: Patterns and Mechanisms. *Annual Review of Marine Science*, **2 (1)**, 115–143, https://doi.org/10.1146/annurev-marine-120408-151453.

Desroziers, G., L. Berre, B. Chapnik, and P. Poli, 2005: Diagnosis of observation, background and analysis-error statistics in observation space. *Quarterly Journal of the Royal Meteorological Society*, **131 (613)**, 3385–3396, https://doi.org/10.1256/qj.05.108.

Doddridge, E. W., and J. Marshall, 2017: Modulation of the Seasonal Cycle of Antarctic Sea Ice Extent Related to the Southern Annular Mode. *Geophysical Research Letters*, **44 (19)**, 9761–9768, https://doi.org/10.1002/2017GL074319.

Dong, Y., K. C. Armour, D. S. Battisti, and E. Blanchard-Wrigglesworth, 2022: Two-Way Teleconnections between the Southern Ocean and the Tropical Pacific via a Dynamic Feedback. *Journal of Climate*, **35 (19)**, 6267–6282, https://doi.org/10.1175/JCLI-D-22-0080.1.

Dong, Y., K. C. Armour, M. D. Zelinka, C. Proistosescu, D. S. Battisti, C. Zhou, and T. Andrews, 2020: Intermodel Spread in the Pattern Effect and Its Contribution to Climate Sensitivity in CMIP5 and CMIP6 Models. *Journal of Climate*, **33 (18)**, 7755–7775, https://doi.org/10.1175/JCLI-D-19-1011.1.

Dong, Y., L. M. Polvani, and D. B. Bonan, 2023: Recent Multi-Decadal Southern Ocean Surface Cooling Unlikely Caused by Southern Annular Mode Trends. *Geophysical Research Letters*, **50 (23)**, https://doi.org/10.1029/2023GL106142.

Dong, Y., C. Proistosescu, K. C. Armour, and D. S. Battisti, 2019: Attributing Historical and Future Evolution of Radiative Feedbacks to Regional Warming Patterns using a Green's Function Approach: The preeminence of the Western Pacific. *Journal of Climate*, https://doi.org/10.1175/JCLI-D-18-0843.1.

Donlon, C. J., M. Martin, J. Stark, J. Roberts-Jones, E. Fiedler, and W. Wimmer, 2012: The Operational Sea Surface Temperature and Sea Ice Analysis (OSTIA) system. *Remote Sensing of Environment*, **116**, 140–158, https://doi.org/10.1016/j.rse.2010.10.017.

Döscher, R., and Coauthors, 2022: The EC-Earth3 Earth system model for the Coupled Model Intercomparison Project 6. *Geoscientific Model Development*, **15 (7)**, 2973–3020, https://doi.org/10.5194/gmd-15-2973-2022.

Dunne, J. P., and Coauthors, 2020: The GFDL Earth System Model Version 4.1 (GFDL-ESM 4.1): Overall Coupled Model Description and Simulation Characteristics. *Journal of Advances in Modeling Earth Systems*, **12 (11)**, https://doi.org/10.1029/2019MS002015.

Edinburgh, T., and J. J. Day, 2016: Estimating the extent of Antarctic summer sea ice during the Heroic Age of Antarctic Exploration. *The Cryosphere*, **10 (6)**, 2721–2730, https://doi.org/10.5194/tc-10-2721-2016.

England, M. R., L. M. Polvani, K. L. Smith, L. Landrum, and M. M. Holland, 2016: Robust response of the Amundsen Sea Low to stratospheric ozone depletion. *Geophysical Research Letters*, **43 (15)**, 8207–8213, https://doi.org/10.1002/2016GL070055.

Espinosa, Z. I., E. Blanchard-Wrigglesworth, and C. M. Bitz, 2024: Understanding the drivers and predictability of record low Antarctic sea ice in austral winter 2023. *Communications Earth & Environment*, **5 (1)**, 723, https://doi.org/10.1038/s43247-024-01772-2.

Evensen, G., 1994: Sequential data assimilation with a nonlinear quasi-geostrophic model using Monte Carlo methods to forecast error statistics. *Journal of Geophysical Research*, **99 (C5)**, https://doi.org/10.1029/94jc00572.

Falster, G., B. Konecky, S. Coats, and S. Stevenson, 2023: Forced changes in the Pacific Walker circulation over the past millennium. *Nature*, https://doi.org/10.1038/s41586-023-06447-0.

Fan, T., C. Deser, and D. P. Schneider, 2014: Recent Antarctic sea ice trends in the context of Southern Ocean surface climate variations since 1950. *Geophysical Research Letters*, **41 (7)**, 2419–2426, https://doi.org/10.1002/2014GL059239.

Flannaghan, T. J., S. Fueglistaler, I. M. Held, S. Po-Chedley, B. Wyman, and M. Zhao, 2014: Tropical temperature trends in Atmospheric General Circulation Model simulations and the impact of uncertainties in observed SSTs. *Journal of Geophysical Research: Atmospheres*, **119 (23)**, 327–340, https://doi.org/10.1002/2014JD022365.

Fogt, R. L., and C. J. Connolly, 2021: Extratropical Southern Hemisphere Synchronous Pressure Variability in the Early Twentieth Century. *Journal of Climate*, **34 (14)**, 5795–5811, https://doi.org/10.1175/JCLI-D-20-0498.1.

Fogt, R. L., and G. J. Marshall, 2020: The Southern Annular Mode: Variability, trends, and climate impacts across the Southern Hemisphere. *WIREs Climate Change*, **11 (4)**, https://doi.org/10.1002/wcc.652.

Fogt, R. L., J. Perlwitz, A. J. Monaghan, D. H. Bromwich, J. M. Jones, and G. J. Marshall, 2009: Historical SAM Variability. Part II: Twentieth-Century Variability and Trends from Reconstructions, Observations, and the IPCC AR4 Models*. *Journal of Climate*, **22 (20)**, 5346–5365, https://doi.org/10.1175/2009JCLI2786.1.

Fogt, R. L., A. M. Sleinkofer, M. N. Raphael, and M. S. Handcock, 2022: A regime shift in seasonal total Antarctic sea ice extent in the twentieth century. *Nature Climate Change*, **12 (1)**, 54–62, https://doi.org/10.1038/s41558-021-01254-9.

Forster, P., and Coauthors, 2021: 2021: The Earth's energy budget, climate feedbacks, and climate sensitivity. *Climate Change 2021: The Physical Science Basis. Contribution of Working Group I to the Sixth Assessment Report of the Intergovernmental Panel on Climate Change*, V. Masson-Delmotte, P. Zhai, A. Pirani, S. Connors, C. Péan, S. Berger, N. Caud, Y. Chen, L. Goldfarb, M. Gomis, M. Huang, K. Leitzell, E. Lonnoy, J. Matthews, T. Maycock, T. Waterfield, O. Yelekçi, R. Yu, and B. Zhou, Eds., Cambridge Univ. Press, Cambridge, UK and New York, NY, chap. 7, https://doi.org/10.1017/9781009157896.009.

Franke, J., S. Brönnimann, J. Bhend, and Y. Brugnara, 2017: A monthly global paleo-reanalysis of the atmosphere from 1600 to 2005 for studying past climatic variations. *Scientific Data*, **4 (1)**, 170 076, https://doi.org/10.1038/sdata.2017.76.

Freeman, E., and Coauthors, 2017: ICOADS Release 3.0: a major update to the historical marine climate record. *International Journal of Climatology*, **37 (5)**, 2211–2232, https://doi.org/10.1002/joc.4775.

Fueglistaler, S., 2019: Observational Evidence for Two Modes of Coupling Between Sea Surface Temperatures, Tropospheric Temperature Profile, and Shortwave Cloud Radiative Effect in the Tropics. *Geophysical Research Letters*, **46 (16)**, 9890–9898, https://doi.org/10.1029/2019GL083990.

Fueglistaler, S., and L. Silvers, 2021: The Peculiar Trajectory of Global Warming. *Journal of Geophysical Research: Atmospheres*, **126 (4)**, 1–15, https://doi.org/10.1029/2020JD033629.

Gong, D., and S. Wang, 1999: Definition of Antarctic Oscillation index. *Geophysical Research Letters*, **26 (4)**, 459–462, https://doi.org/10.1029/1999GL900003.

Hakim, G. J., J. Emile-Geay, E. J. Steig, D. Noone, D. M. Anderson, R. Tardif, N. Steiger, and W. A. Perkins, 2016: The last millennium climate reanalysis project: Framework and first results. *Journal of Geophysical Research: Atmospheres*, **121 (12)**, 6745–6764, https://doi.org/10.1002/2016JD024751.

Hakim, G. J., C. Snyder, S. G. Penny, and M. Newman, 2022: Subseasonal Forecast Skill Improvement From Strongly Coupled Data Assimilation With a Linear Inverse Model. *Geophysical Research Letters*, **49 (11)**, https://doi.org/10.1029/2022GL097996.

Hartmann, D. L., 2022: The Antarctic ozone hole and the pattern effect on climate sensitivity. *Proceedings of the National Academy of Sciences*, **119 (35)**, https://doi.org/10.1073/pnas.2207889119.

Hasselmann, K., 1976: Stochastic climate models: Part I. Theory. *Tellus A: Dynamic Meteorology and Oceanography*, **28 (6)**, 473, https://doi.org/10.3402/tellusa.v28i6.11316.

Hausfather, Z., K. Cowtan, D. C. Clarke, P. Jacobs, M. Richardson, and R. Rohde, 2017: Assessing recent warming using instrumentally homogeneous sea surface temperature records. *Science Advances*, **3 (1)**, https://doi.org/10.1126/SCIADV.1601207/SUPPL{_}FILE/1601207{_}SM.PDF.

Heede, U. K., and A. V. Fedorov, 2023: Colder Eastern Equatorial Pacific and Stronger Walker Circulation in the Early 21st Century: Separating the Forced Response to Global Warming From Natural Variability. *Geophysical Research Letters*, **50 (3)**, https://doi.org/10.1029/2022GL101020.

Hegerl, G. C., S. Brönnimann, A. Schurer, and T. Cowan, 2018: The early 20th century warming: Anomalies, causes, and consequences. *WIREs Climate Change*, **9 (4)**, https://doi.org/10.1002/wcc.522.

Hegerl, G. C., and Coauthors, 2019: Causes of climate change over the historical record. *Environmental Research Letters*, **14 (12)**, 123 006, https://doi.org/10.1088/1748-9326/AB4557.

Hersbach, H., and Coauthors, 2020: The ERA5 global reanalysis. *Quarterly Journal of the Royal Meteorological Society*, **146 (730)**, 1999–2049, https://doi.org/10.1002/qj.3803.

Hirahara, S., M. Ishii, and Y. Fukuda, 2014: Centennial-Scale Sea Surface Temperature Analysis and Its Uncertainty. *Journal of Climate*, **27 (1)**, 57–75, https://doi.org/10.1175/JCLI-D-12-00837.1.

Houtekamer, P. L., and H. L. Mitchell, 1998: Data Assimilation Using an Ensemble Kalman Filter Technique. *Monthly Weather Review*, **126 (3)**, 796–811, https://doi.org/10.1175/1520-0493(1998)126⟨0796:DAUAEK⟩2.0.CO;2.

Houtekamer, P. L., and F. Zhang, 2016: Review of the Ensemble Kalman Filter for Atmospheric Data Assimilation. *Monthly Weather Review*, **144 (12)**, 4489–4532, https://doi.org/10.1175/MWR-D-15-0440.1.

Huang, B., C. Liu, G. Ren, H. M. Zhang, and L. Zhang, 2019: The Role of Buoy and Argo Observations in Two SST Analyses in the Global and Tropical Pacific Oceans. *Journal of Climate*, **32 (9)**, 2517–2535, https://doi.org/10.1175/JCLI-D-18-0368.1.

Huang, B., and Coauthors, 2017: Extended Reconstructed Sea Surface Temperature, Version 5 (ERSSTv5): Upgrades, Validations, and Intercomparisons. *Journal of Climate*, **30 (20)**, 8179–8205, https://doi.org/10.1175/JCLI-D-16-0836.1.

Hurrell, J. W., J. J. Hack, D. Shea, J. M. Caron, and J. Rosinski, 2008: A New Sea Surface Temperature and Sea Ice Boundary Dataset for the Community Atmosphere Model. *Journal of Climate*, **21 (19)**, 5145–5153, https://doi.org/10.1175/2008JCLI2292.1.

Kadow, C., D. M. Hall, and U. Ulbrich, 2020: Artificial intelligence reconstructs missing climate information. *Nature Geoscience*, **13 (6)**, 408–413, https://doi.org/10.1038/s41561-020-0582-5.

Kalman, R. E., 1960: A New Approach to Linear Filtering and Prediction Problems. *Journal of Basic Engineering*, **82 (1)**, 35–45, https://doi.org/10.1115/1.3662552.

Kalnay, E., 2003: *Atmospheric Modeling, Data Assimilation and Predictability*. Cambridge University Press.

Kalnay, E., and Coauthors, 1996: The NCEP/NCAR 40-year reanalysis project. *Bulletin of the American Meteorological Society*, **77 (3)**, https://doi.org/10.1175/1520-0477(1996)077⟨0437:TNYRP⟩2.0.CO;2.

Kang, J. M., T. A. Shaw, S. M. Kang, I. R. Simpson, and Y. Yu, 2024: Revisiting the reanalysis-model discrepancy in Southern Hemisphere winter storm track trends. *npj Climate and Atmospheric Science*, **7 (1)**, 252, https://doi.org/10.1038/s41612-024-00801-3.

Kang, S. M., P. Ceppi, Y. Yu, and I.-S. Kang, 2023a: Recent global climate feedback controlled by Southern Ocean cooling. *Nature Geoscience*, https://doi.org/10.1038/s41561-023-01256-6.

Kang, S. M., Y. Yu, C. Deser, X. Zhang, I.-S. Kang, S.-S. Lee, K. B. Rodgers, and P. Ceppi, 2023b: Global impacts of recent Southern Ocean cooling. *Proceedings of the National Academy of Sciences*, **120 (30)**, https://doi.org/10.1073/pnas.2300881120.

Kaplan, A., M. A. Cane, Y. Kushnir, A. C. Clement, M. B. Blumenthal, and B. Rajagopalan, 1998: Analyses of global sea surface temperature 1856–1991. *Journal of Geophysical Research: Oceans*, **103 (C9)**, 18 567–18 589, https://doi.org/10.1029/97JC01736.

Kaplan, A., Y. Kushnir, and M. A. Cane, 2000: Reduced Space Optimal Interpolation of Historical Marine Sea Level Pressure: 1854–1992*. *Journal of Climate*, **13 (16)**, 2987–3002, https://doi.org/10.1175/1520-0442(2000)013⟨2987:RSOIOH⟩2.0.CO;2.

Karl, T. R., and Coauthors, 2015: Possible artifacts of data biases in the recent global surface warming hiatus. *Science*, **348 (6242)**, 1469–1472, https://doi.org/10.1126/SCIENCE.AAA5632/SUPPL{_}FILE/PAPV2.PDF.

Kennedy, J. J., 2014: A review of uncertainty in in situ measurements and data sets of sea surface temperature. *Reviews of Geophysics*, **52 (1)**, 1–32, https://doi.org/10.1002/2013RG000434.

Kennedy, J. J., N. A. Rayner, C. P. Atkinson, and R. E. Killick, 2019: An Ensemble Data Set of Sea Surface Temperature Change From 1850: The Met Office Hadley Centre HadSST.4.0.0.0 Data Set. *Journal of Geophysical Research: Atmospheres*, **124 (14)**, 7719–7763, https://doi.org/10.1029/2018JD029867.

Kent, E. C., and J. J. Kennedy, 2021: Historical Estimates of Surface Marine Temperatures. *Annual Review of Marine Science*, **13 (1)**, 283–311, https://doi.org/10.1146/annurev-marine-042120-111807.

Kido, S., I. Richter, T. Tozuka, and P. Chang, 2023: Understanding the interplay between ENSO and related tropical SST variability using linear inverse models. *Climate Dynamics*, **61 (3-4)**, 1029–1048, https://doi.org/10.1007/s00382-022-06484-x.

King, J., K. J. Anchukaitis, K. Allen, T. Vance, and A. Hessl, 2023: Trends and variability in the Southern Annular Mode over the Common Era. *Nature Communications*, **14 (1)**, 2324, https://doi.org/10.1038/s41467-023-37643-1.

KOBAYASHI, S., and Coauthors, 2015: The JRA-55 Reanalysis: General Specifications and Basic Characteristics. *Journal of the Meteorological Society of Japan. Ser. II*, **93 (1)**, 5–48, https://doi.org/10.2151/jmsj.2015-001.

Kohyama, T., and D. L. Hartmann, 2016: Antarctic Sea Ice Response to Weather and Climate Modes of Variability*. *Journal of Climate*, **29 (2)**, 721–741, https://doi.org/10.1175/JCLI-D-15-0301.1.

Kuhlbrodt, T., and Coauthors, 2018: The Low-Resolution Version of HadGEM3 GC3.1: Development and Evaluation for Global Climate. *Journal of Advances in Modeling Earth Systems*, **10 (11)**, 2865–2888, https://doi.org/10.1029/2018MS001370.

Laloyaux, P., and Coauthors, 2018: CERA-20C: A Coupled Reanalysis of the Twentieth Century. *Journal of Advances in Modeling Earth Systems*, **10 (5)**, 1172–1195, https://doi.org/10.1029/2018MS001273.

Lee, S., M. L'Heureux, A. T. Wittenberg, R. Seager, P. A. O'Gorman, and N. C. Johnson, 2022: On the future zonal contrasts of equatorial Pacific climate: Perspectives from Observations, Simulations, and Theories. *npj Climate and Atmospheric Science*, **5 (1)**, 82, https://doi.org/10.1038/s41612-022-00301-2.

Leith, C. E., 1973: The Standard Error of Time-Average Estimates of Climatic Means. *Journal of Applied Meteorology*, **12 (6)**, 1066–1069, https://doi.org/10.1175/1520-0450(1973)012⟨1066:TSEOTA⟩2.0.CO;2.

Lewis, N., and T. Mauritsen, 2021: Negligible Unforced Historical Pattern Effect on Climate Feedback Strength Found in HadISST-Based AMIP Simulations. *Journal of Climate*, **34 (1)**, 39–55, https://doi.org/10.1175/JCLI-D-19-0941.1.

Lin, Y., and Coauthors, 2020: Community Integrated Earth System Model (CIESM): Description and Evaluation. *Journal of Advances in Modeling Earth Systems*, **12 (8)**, e2019MS002 036, https://doi.org/10.1029/2019MS002036.

Lou, J., M. Newman, and A. Hoell, 2023: Multi-decadal variation of ENSO forecast skill since the late 1800s. *npj Climate and Atmospheric Science*, **6 (1)**, 89, https://doi.org/10.1038/s41612-023-00417-z.

L'Heureux, M. L., S. Lee, and B. Lyon, 2013: Recent multidecadal strengthening of the Walker circulation across the tropical Pacific. *Nature Climate Change*, **3 (6)**, 571–576, https://doi.org/10.1038/nclimate1840.

Marshall, G. J., 2003: Trends in the Southern Annular Mode from Observations and Reanalyses. *Journal of Climate*, **16 (24)**, 4134–4143, https://doi.org/10.1175/1520-0442(2003)016⟨4134:TITSAM⟩2.0.CO;2.

Marvel, K., R. Pincus, G. A. Schmidt, and R. L. Miller, 2018: Internal Variability and Disequilibrium Confound Estimates of Climate Sensitivity From Observations. *Geophysical Research Letters*, **45 (3)**, 1595–1601, https://doi.org/10.1002/2017GL076468.

Mauritsen, T., and Coauthors, 2019: Developments in the MPI-M Earth System Model version 1.2 (MPI-ESM1.2) and Its Response to Increasing CO¡sub¿2¡/sub¿. *Journal of Advances in Modeling Earth Systems*, **11 (4)**, 998–1038, https://doi.org/10.1029/2018MS001400.

McGregor, S., A. Timmermann, M. F. Stuecker, M. H. England, M. Merrifield, F.-F. Jin, and Y. Chikamoto, 2014: Recent Walker circulation strengthening and Pacific cooling amplified by Atlantic warming. *Nature Climate Change*, **4 (10)**, 888–892, https://doi.org/10.1038/nclimate2330.

Meier, W. N., F. Fetterer, A. K. Windnagel, and J. S. Stewart, 2021a: Near-Real-Time NOAA/NSIDC Climate Data Record of Passive Microwave Sea Ice Concentration (G10016, Version 2). Tech. rep., NSIDC: National Snow and Ice Data Center, Boulder, CO. https://doi.org/10.7265/tgam-yv28.

Meier, W. N., F. Fetterer, A. K. Windnagel, and J. S. Stewart, 2021b: NOAA/NSIDC Climate Data Record of Passive Microwave Sea Ice Concentration, Version 4. Tech. rep., NSIDC: National Snow and Ice Data Center, Boulder, Colorado USA. https://doi.org/https://doi.org/10.7265/efmz-2t65.

Meng, Z., and G. J. Hakim, 2024: Reconstructing the Tropical Pacific Upper Ocean Using Online Data Assimilation With a Deep Learning Model. *Journal of Advances in Modeling Earth Systems*, **16 (11)**, https://doi.org/10.1029/2024MS004422.

Modak, A., and T. Mauritsen, 2023: Better-constrained climate sensitivity when accounting for dataset dependency on pattern effect estimates. *Atmospheric Chemistry and Physics*, **23 (13)**, 7535–7549, https://doi.org/10.5194/acp-23-7535-2023.

Morice, C. P., and Coauthors, 2021: An Updated Assessment of Near-Surface Temperature Change From 1850: The HadCRUT5 Data Set. *Journal of Geophysical Research: Atmospheres*, **126 (3)**, https://doi.org/10.1029/2019JD032361.

Nash, J. E., and J. V. Sutcliffe, 1970: River flow forecasting through conceptual models part I — A discussion of principles. *Journal of Hydrology*, **10 (3)**, 282–290, https://doi.org/10.1016/0022-1694(70)90255-6.

Newman, M., 2007: Interannual to Decadal Predictability of Tropical and North Pacific Sea Surface Temperatures. *Journal of Climate*, **20 (11)**, 2333–2356, https://doi.org/10.1175/JCLI4165.1.

Newman, M., 2013: An Empirical Benchmark for Decadal Forecasts of Global Surface Temperature Anomalies. *Journal of Climate*, **26 (14)**, 5260–5269, https://doi.org/10.1175/JCLI-D-12-00590.1.

Newman, M., and Coauthors, 2016: The Pacific Decadal Oscillation, Revisited. *Journal of Climate*, **29 (12)**, 4399–4427, https://doi.org/10.1175/JCLI-D-15-0508.1.

OrtizBeviá, M. J., 1997: Estimation of the cyclostationary dependence in geophysical data fields. *Journal of Geophysical Research: Atmospheres*, **102 (D12)**, 13 473–13 486, https://doi.org/10.1029/97JD00243.

Osborn, T. J., P. D. Jones, D. H. Lister, C. P. Morice, I. R. Simpson, J. P. Winn, E. Hogan, and I. C. Harris, 2021: Land Surface Air Temperature Variations Across the Globe Updated to 2019: The CRUTEM5 Data Set. *Journal of Geophysical Research: Atmospheres*, **126 (2)**, https://doi.org/10.1029/2019JD032352.

Osman, M. B., J. E. Tierney, J. Zhu, R. Tardif, G. J. Hakim, J. King, and C. J. Poulsen, 2021: Globally resolved surface temperatures since the Last Glacial Maximum. *Nature*, **599 (7884)**, 239–244, https://doi.org/10.1038/s41586-021-03984-4.

O'Connor, G. K., E. J. Steig, and G. J. Hakim, 2021: Strengthening Southern Hemisphere Westerlies and Amundsen Sea Low Deepening Over the 20th Century Revealed by Proxy-Data Assimilation. *Geophysical Research Letters*, **48 (24)**, e2021GL095 999, https://doi.org/10.1029/2021GL095999.

Park, S., J. Shin, S. Kim, E. Oh, and Y. Kim, 2019: Global Climate Simulated by the Seoul National University Atmosphere Model Version 0 with a Unified Convection Scheme (SAM0-UNICON). *Journal of Climate*, **32 (10)**, 2917–2949, https://doi.org/10.1175/JCLI-D-18-0796.1.

Parsons, L. A., D. E. Amrhein, S. C. Sanchez, R. Tardif, M. K. Brennan, and G. J. Hakim, 2021: Do Multi-Model Ensembles Improve Reconstruction Skill in Paleoclimate Data Assimilation? *Earth and Space Science*, **8 (4)**, e2020EA001 467, https://doi.org/10.1029/2020EA001467.

Penland, C., 1989: Random Forcing and Forecasting Using Principal Oscillation Pattern Analysis. *Monthly Weather Review*, **117 (10)**, 2165–2185, https://doi.org/10.1175/1520-0493(1989)117⟨2165:RFAFUP⟩2.0.CO;2.

Penland, C., 1996: A stochastic model of IndoPacific sea surface temperature anomalies. *Physica D: Nonlinear Phenomena*, **98 (2-4)**, 534–558, https://doi.org/10.1016/0167-2789(96)00124-8.

Penland, C., and L. Matrosova, 1994: A Balance Condition for Stochastic Numerical Models with Application to the El Niño-Southern Oscillation. *Journal of Climate*, **7 (9)**, 1352–1372, https://doi.org/https://doi.org/10.1175/1520-0442(1994)007{\%}3C1352:ABCFSN{\% }3E2.0.CO;2.

Penland, C., and P. D. Sardeshmukh, 1995: The Optimal Growth of Tropical Sea Surface Temperature Anomalies. *Journal of Climate*, **8 (8)**, 1999–2024, https://doi.org/10.1175/1520-0442(1995)008⟨1999:TOGOTS⟩2.0.CO;2.

Perkins, W. A., and G. J. Hakim, 2021: Coupled Atmosphere–Ocean Reconstruction of the Last Millennium Using Online Data Assimilation. *Paleoceanography and Paleoclimatology*, **36 (5)**, https://doi.org/10.1029/2020PA003959.

Polvani, L. M., and Coauthors, 2021: Interannual SAM Modulation of Antarctic Sea Ice Extent Does Not Account for Its Long-Term Trends, Pointing to a Limited Role for Ozone Depletion. *Geophysical Research Letters*, **48 (21)**, https://doi.org/10.1029/2021GL094871.

Purich, A., W. Cai, M. H. England, and T. Cowan, 2016: Evidence for link between modelled trends in Antarctic sea ice and underestimated westerly wind changes. *Nature Communications*, **7 (1)**, 10 409, https://doi.org/10.1038/ncomms10409.

Qin, Y., X. Zheng, S. A. Klein, M. D. Zelinka, P. Ma, J. Golaz, and S. Xie, 2024: Causes of Reduced Climate Sensitivity in E3SM From Version 1 to Version 2. *Journal of Advances in Modeling Earth Systems*, **16 (1)**, https://doi.org/10.1029/2023MS003875.

Rayner, N. A., D. E. Parker, E. B. Horton, C. K. Folland, L. V. Alexander, D. P. Rowell, E. C. Kent, and A. Kaplan, 2003: Global analyses of sea surface temperature, sea ice, and night marine air temperature since the late nineteenth century. *Journal of Geophysical Research: Atmospheres*, **108 (14)**, https://doi.org/10.1029/2002jd002670.

Roach, L. A., and W. N. Meier, 2024: Sea ice in 2023. *Nature Reviews Earth & Environment*, **5 (4)**, 235–237, https://doi.org/10.1038/s43017-024-00542-0.

Roach, L. A., and Coauthors, 2020: Antarctic Sea Ice Area in CMIP6. *Geophysical Research Letters*, **47 (9)**, https://doi.org/10.1029/2019GL086729.

Rohde, R., and Coauthors, 2013: An Overview Berkeley Earth Temperature Averaging Process. *Geoinformatics & Geostatistics: An Overview*, **(June)**, https://doi.org/10.4172/gigs.1000103.

Salvi, P., J. M. Gregory, and P. Ceppi, 2023: Time-Evolving Radiative Feedbacks in the Historical Period. *Journal of Geophysical Research: Atmospheres*, **128 (20)**, https://doi.org/10.1029/2023JD038984.

Schneider, T., 2001: Analysis of Incomplete Climate Data: Estimation of Mean Values and Covariance Matrices and Imputation of Missing Values. *Journal of Climate*, **14 (5)**, 853–871, https://doi.org/10.1175/1520-0442(2001)014⟨0853:AOICDE⟩2.0.CO;2.

Schneider, T., and I. M. Held, 2001: Discriminants of Twentieth-Century Changes in Earth Surface Temperatures. *Journal of Climate*, **14 (3)**, 249–254, https://doi.org/10.1175/1520-0442(2001)014⟨0249:LDOTCC⟩2.0.CO;2.

Screen, J. A., 2011: Sudden increase in Antarctic sea ice: Fact or artifact? *Geophysical Research Letters*, **38 (13)**, n/a–n/a, https://doi.org/10.1029/2011GL047553.

Seland, , and Coauthors, 2020: Overview of the Norwegian Earth System Model (NorESM2) and key climate response of CMIP6 DECK, historical, and scenario simulations. *Geoscientific Model Development*, **13 (12)**, 6165–6200, https://doi.org/10.5194/gmd-13-6165-2020.

Sellar, A. A., and Coauthors, 2019: UKESM1: Description and Evaluation of the U.K. Earth System Model. *Journal of Advances in Modeling Earth Systems*, **11 (12)**, 4513–4558, https://doi.org/10.1029/2019MS001739.

Seviour, W. J. M., A. Gnanadesikan, and D. W. Waugh, 2016: The Transient Response of the Southern Ocean to Stratospheric Ozone Depletion. *Journal of Climate*, **29 (20)**, 7383–7396, https://doi.org/10.1175/JCLI-D-16-0198.1.

Sherwood, S. C., and Coauthors, 2020: An Assessment of Earth's Climate Sensitivity Using Multiple Lines of Evidence. *Reviews of Geophysics*, **58 (4)**, https://doi.org/10.1029/2019RG000678.

Shin, S.-I., P. D. Sardeshmukh, M. Newman, C. Penland, and M. A. Alexander, 2021: Impact of Annual Cycle on ENSO Variability and Predictability. *Journal of Climate*, **34 (1)**, 171–193, https://doi.org/10.1175/JCLI-D-20-0291.1.

Sippel, S., and Coauthors, 2024: Early-twentieth-century cold bias in ocean surface temperature observations. *Nature*, **635 (8039)**, 618–624, https://doi.org/10.1038/s41586-024-08230-1.

Slivinski, L. C., and Coauthors, 2019: Towards a more reliable historical reanalysis: Improvements for version 3 of the Twentieth Century Reanalysis system. *Quarterly Journal of the Royal Meteorological Society*, **145 (724)**, 2876–2908, https://doi.org/10.1002/qj.3598.

Smerdon, J. E., E. R. Cook, and N. J. Steiger, 2023: The Historical Development of Large-Scale Paleoclimate Field Reconstructions Over the Common Era. *Reviews of Geophysics*, **61 (4)**, https://doi.org/10.1029/2022RG000782.

Solomon, A., and M. Newman, 2012: Reconciling disparate twentieth-century Indo-Pacific ocean temperature trends in the instrumental record. *Nature Climate Change*, **2 (9)**, 691–699, https://doi.org/10.1038/nclimate1591.

Steiger, N. J., G. J. Hakim, E. J. Steig, D. S. Battisti, and G. H. Roe, 2014: Assimilation of time-averaged pseudoproxies for climate reconstruction. *Journal of Climate*, **27 (1)**, https://doi.org/10.1175/JCLI-D-12-00693.1.

Steiger, N. J., J. E. Smerdon, E. R. Cook, and B. I. Cook, 2018: A reconstruction of global hydroclimate and dynamical variables over the Common Era. *Scientific Data*, **5 (1)**, 180 086, https://doi.org/10.1038/sdata.2018.86.

Stuecker, M. F., C. M. Bitz, and K. C. Armour, 2017: Conditions leading to the unprecedented low Antarctic sea ice extent during the 2016 austral spring season. *Geophysical Research Letters*, **44 (17)**, 9008–9019, https://doi.org/10.1002/2017GL074691.

Swart, N. C., J. C. Fyfe, N. Gillett, and G. J. Marshall, 2015: Comparing Trends in the Southern Annular Mode and Surface Westerly Jet. *Journal of Climate*, **28 (22)**, 8840–8859, https://doi.org/10.1175/JCLI-D-15-0334.1.

Thomas, J. L., D. W. Waugh, and A. Gnanadesikan, 2015: Southern Hemisphere extratropical circulation: Recent trends and natural variability. *Geophysical Research Letters*, **42 (13)**, 5508–5515, https://doi.org/10.1002/2015GL064521.

Thompson, D. W. J., S. Solomon, P. J. Kushner, M. H. England, K. M. Grise, and D. J. Karoly, 2011: Signatures of the Antarctic ozone hole in Southern Hemisphere surface climate change. *Nature Geoscience*, **4 (11)**, 741–749, https://doi.org/10.1038/ngeo1296.

Tierney, J. E., J. Zhu, J. King, S. B. Malevich, G. J. Hakim, and C. J. Poulsen, 2020: Glacial cooling and climate sensitivity revisited. *Nature*, **584 (7822)**, 569–573, https://doi.org/10.1038/s41586-020-2617-x.

Titchner, H. A., and N. A. Rayner, 2014: The Met Office Hadley Centre sea ice and sea surface temperature data set, version 2: 1. Sea ice concentrations. *Journal of Geophysical Research: Atmospheres*, **119 (6)**, 2864–2889, https://doi.org/10.1002/2013JD020316.

Tokinaga, H., S.-P. Xie, A. Timmermann, S. McGregor, T. Ogata, H. Kubota, and Y. M. Okumura, 2012: Regional Patterns of Tropical Indo-Pacific Climate Change: Evidence of the Walker Circulation Weakening. *Journal of Climate*, **25 (5)**, 1689–1710, https://doi.org/10.1175/JCLI-D-11-00263.1.

Trenberth, K. E., and D. J. Shea, 2006: Atlantic hurricanes and natural variability in 2005. *Geophysical Research Letters*, **33 (12)**, 12 704, https://doi.org/10.1029/2006GL026894.

Tseng, K.-C., N. C. Johnson, E. D. Maloney, E. A. Barnes, and S. B. Kapnick, 2021: Mapping Large-Scale Climate Variability to Hydrological Extremes: An Application of the Linear Inverse Model to Subseasonal Prediction. *Journal of Climate*, **34 (11)**, 4207–4225, https://doi.org/10.1175/JCLI-D-20-0502.1.

Turner, J., and Coauthors, 2022: Record Low Antarctic Sea Ice Cover in February 2022. *Geophysical Research Letters*, **49 (12)**, https://doi.org/10.1029/2022GL098904.

Vaccaro, A., J. Emile-Geay, D. Guillot, R. Verna, C. Morice, J. Kennedy, and B. Rajaratnam, 2021: Climate Field Completion via Markov Random Fields: Application to the HadCRUT4.6 Temperature Dataset. *Journal of Climate*, **34 (10)**, 4169–4188, https://doi.org/10.1175/JCLI-D-19-0814.1.

Valler, V., and Coauthors, 2024: ModE-RA: a global monthly paleo-reanalysis of the modern era 1421 to 2008. *Scientific Data*, **11 (1)**, 36, https://doi.org/10.1038/s41597-023-02733-8.

Vecchi, G. A., B. J. Soden, A. T. Wittenberg, I. M. Held, A. Leetmaa, and M. J. Harrison, 2006: Weakening of tropical Pacific atmospheric circulation due to anthropogenic forcing. *Nature*, **441 (7089)**, 73–76, https://doi.org/10.1038/nature04744.

Vimont, D. J., 2012: Analysis of the Atlantic Meridional Mode Using Linear Inverse Modeling: Seasonality and Regional Influences. *Journal of Climate*, **25 (4)**, 1194–1212, https://doi.org/10.1175/JCLI-D-11-00012.1.

Vimont, D. J., M. A. Alexander, and M. Newman, 2014: Optimal growth of Central and East Pacific ENSO events. *Geophysical Research Letters*, **41 (11)**, 4027–4034, https://doi.org/10.1002/2014GL059997.

Vimont, D. J., M. Newman, D. S. Battisti, and S.-I. Shin, 2022: The Role of Seasonality and the ENSO Mode in Central and East Pacific ENSO Growth and Evolution. *Journal of Climate*, **35 (11)**, 3195–3209, https://doi.org/10.1175/JCLI-D-21-0599.1.

Walsh, J. E., W. L. Chapman, F. Fetterer, and S. Stewart, 2019: Gridded Monthly Sea Ice Extent and Concentration, 1850 Onward, Version 2. Tech. rep., NSIDC: National Snow and Ice Data Center., Boulder, Colorado USA. https://doi.org/10.7265/jj4s-tq79, URL https://dx.doi.org/10.7265/jj4s-tq79.

Walsh, J. E., F. Fetterer, J. Scott stewart, and W. L. Chapman, 2017: A database for depicting Arctic sea ice variations back to 1850. *Geographical Review*, **107 (1)**, 89–107, https://doi.org/10.1111/j.1931-0846.2016.12195.x.

Watanabe, M., T. Iwakiri, Y. Dong, and S. M. Kang, 2023: Two Competing Drivers of the Recent Walker Circulation Trend. *Geophysical Research Letters*, **50 (23)**, e2023GL105 332, https://doi.org/10.1029/2023GL105332.

Watanabe, M., S. M. Kang, M. Collins, Y.-T. Hwang, S. McGregor, and M. F. Stuecker, 2024: Possible shift in controls of the tropical Pacific surface warming pattern. *Nature*, **630 (8016)**, 315–324, https://doi.org/10.1038/s41586-024-07452-7.

Webb, M. J., and Coauthors, 2017: The Cloud Feedback Model Intercomparison Project (CFMIP) contribution to CMIP6. *Geoscientific Model Development*, **10 (1)**, 359–384, https://doi.org/10.5194/gmd-10-359-2017.

Wills, R. C. J., Y. Dong, C. Proistosecu, K. C. Armour, and D. S. Battisti, 2022: Systematic Climate Model Biases in the Large-Scale Patterns of Recent Sea-Surface Temperature and Sea-Level Pressure Change. *Geophysical Research Letters*, **49 (17)**, e2022GL100 011, https://doi.org/10.1029/2022GL100011.

Wunsch, C., 1999: The Interpretation of Short Climate Records, with Comments on the North Atlantic and Southern Oscillations. *Bulletin of the American Meteorological Society*, **80 (2)**, 245–255, https://doi.org/10.1175/1520-0477(1999)080⟨0245:TIOSCR⟩2.0.CO;2.

Zanna, L., 2012: Forecast Skill and Predictability of Observed Atlantic Sea Surface Temperatures. *Journal of Climate*, **25 (14)**, 5047–5056, https://doi.org/10.1175/JCLI-D-11-00539.1.

Zhang, C., and S. Li, 2023: Causes of the record-low Antarctic sea-ice in austral summer 2022. *Atmospheric and Oceanic Science Letters*, **16 (6)**, 100 353, https://doi.org/10.1016/j.aosl.2023.100353.

Zhang, X., C. Deser, and L. Sun, 2021: Is There a Tropical Response to Recent Observed Southern Ocean Cooling? *Geophysical Research Letters*, **48 (5)**, https://doi.org/10.1029/2020GL091235.

Zhao, Y., D. Sun, E. Di Lorenzo, G. Liu, and S. Wu, 2024: Separate the Role of Southern and Northern Extra-Tropical Pacific in Tropical Pacific Climate Variability. *Geophysical Research Letters*, **51 (16)**, https://doi.org/10.1029/2024GL109466.

Zhou, C., M. D. Zelinka, and S. A. Klein, 2016: Impact of decadal cloud variations on the Earth's energy budget. *Nature Geoscience*, **9 (12)**, 871–874, https://doi.org/10.1038/ngeo2828.